

1 **BAYESIAN PHYSICAL-STATISTICAL RETRIEVAL OF SWE AND SNOW DEPTH FROM X**
2 **AND KU-BAND SAR - DEMONSTRATION USING AIRBORNE SNOWSAR IN SNOWEX'17**

3 Siddharth Singh¹, Michael Durand,² Edward Kim³, Ana P. Barros¹

4
5 ¹Department of Civil and Environmental Engineering, University of Illinois at Urbana-
6 Champaign, Urbana, Illinois, USA

7 ²School of Earth Sciences, Ohio State University, Columbus, Ohio, USA

8 ³NASA Goddard Space Flight Center, Greenbelt, Maryland, USA

9 *Correspondence to:* Ana P. Barros (barros@illinois.edu)

10 **Abstract**

11 A physical-statistical framework to estimate Snow Water Equivalent (SWE) and snow depth from
12 SAR measurements is presented and applied to four SnowSAR flight-line data sets collected
13 during the SnowEx'2017 field campaign in Grand Mesa, Colorado, USA. The physical (radar)
14 model is used to describe the relationship between snowpack conditions and volume backscatter.
15 The statistical model is a Bayesian inference model that seeks to estimate the joint probability
16 distribution of volume backscatter measurements, snow density and snow depth, and physical
17 model parameters. Prior distributions are derived from multilayer snow hydrology predictions
18 driven by downscaled numerical weather prediction (NWP) forecasts. To reduce noise to signal
19 ratio, SnowSAR measurements at 1 m resolution were upscaled by simple averaging to 30 and 90
20 m resolution. To reduce the number of physical parameters, the multilayer snowpack is
21 transformed for Bayesian inference into an equivalent single- or two-layer snowpack with the same
22 snow mass and volume backscatter. Successful retrievals meeting NASEM (2018) science
23 requirements are defined by absolute convergence backscatter errors ≤ 1.2 dB and local SnowSAR
24 incidence angles between 30° and 45° for X- and Ku-band VV-pol backscatter measurements and
25 were achieved for 75% to 87% for all grassland pixels with SWE up to 0.7m and snow depth up
26 to 2 m. SWE retrievals compare well with snow pit observations showing strong skill in deep snow
27 with average absolute SWE residuals of 5-7% (15-18%) for the two-layer (single-layer) retrieval
28 algorithm. Furthermore, the spatial distributions of snow depth retrievals vis-à-vis LIDAR
29 estimates have Bhattacharya Coefficients above 94% (90%) for homogeneous grassland pixels at
30 30 m (90 m resolution), and values up to 76% in mixed forest and grassland areas indicating that
31 the retrievals closely capture snowpack spatial variability. Because NWP forecasts are available
32 everywhere, the proposed approach could be applied to SWE and snow depth retrievals from a
33 dedicated global snow mission.

34

35 1. Introduction

36 The seasonal snowpack plays a critical role in climate and weather variability due to its role in the
37 surface energy budget on account of its high albedo, and in the surface water budget as temporary
38 storage of frozen precipitation in the cold season until it melts in the warm season and becomes
39 available as runoff. The water stored in the snowpack is measured by the Snow Water Equivalent
40 (SWE), the depth of liquid water per unit area that would be released if the snowpack were to melt
41 completely. It is the product of the specific gravity of snow with respect to water ($\rho_{\text{snow}}/\rho_{\text{w}}$) and
42 the depth of the snowpack (SD). To map SWE in the cold season is to map snow water resources.
43 To map onset of melt and snow wetness is to map the timing and geography of snow water
44 resources availability. Climate variability and change with increasing air temperature, shifts in
45 atmospheric moisture convergence patterns, and increases in the frequency of extreme events is
46 already causing significant changes in frequency and patterns and timing of seasonal snow
47 accumulation and melt with severe implications for water and food security in addition to
48 cascading economic and ecosystem impacts (Huang and Swain, 2022; Musselman et al., 2021;
49 Sturm et al., 2010).

50 The need to capture snowpack heterogeneity and dynamics tied to weather, climate, landcover and
51 landform variability remains a chief challenge to developing a snow observing system at the spatial
52 and temporal scales required to answer water cycle science questions and for societal decision-
53 making. The potential for systematic snowpack monitoring in remote regions has long been
54 investigated, including the integration of remote sensing measurements and physical models (e.g.
55 (Martinec et al. 1991; Mote et al. 2003; Bateni et al. 2015; Li et al. 2017; Kim et al. 2019; Cao and
56 Barros, 2023a). Assimilation of radiance or backscatter is most powerful with a time series of
57 observations. Time-series observations are available presently from tower measurements, albeit
58 at the point scale of the tower footprint (see summary by Tsang et al. 2022), and do not capture
59 the large joint spatial and temporal variability of snowpacks from local to regional scales
60 depending on weather and climate, landform, land use and landcover. Frequent spatial
61 observations are required for this purpose. Airborne observations can be used for mapping but
62 typically occur once or twice during a winter season and over limited areas. A dedicated satellite
63 mission is necessary to acquire time-series of measurements globally.

64 Presently, advances in radar technology and retrieval algorithms (Tsang et al., 2022), and
65 especially the demonstrated capabilities of NewSpace satellite missions (Villano et al. 2020) make
66 high spatial resolution of Synthetic Aperture Radar (SAR; 10's m) Earth observations from space
67 feasible in contrast to the challenges faced in the past (Rott et al. 2012). During the SnowEx'17
68 field campaign (Kim et al., 2017), a comprehensive data set consisting of airborne dual-frequency
69 SAR (X- and Ku-band Synthetic Aperture Radar) backscatter measurements using the SnowSAR
70 instrument (Macedo et al. 2020), the Airborne Snow Observatory (ASO, Painter et al. 2018) and a
71 plethora of high-quality ground-validation measurements of snowpack properties and ancillary
72 data (Table 1) offer an unprecedented opportunity to investigate the full potential of SAR toward
73 developing the next generation of retrieval algorithms.

74 Due to the highly nonlinear snow physics and the time-varying stratigraphy of snowpacks,
75 radiance or backscatter measurements depend on the vertical structure of snowpack physical
76 properties such as snow density, snow temperature, and snow grain size in addition to SWE and

77 snow depth. Because the number of observations is smaller than the number of parameters required
78 to solve the inverse-problem, retrieval of SWE and snow depth is an underdetermined estimation
79 problem. This challenge can be addressed using a physical-statistical approach for retrieval.
80 Physical-statistical approaches combine physical process models with a Bayesian statistical
81 framework to inform how geophysical states and parameters relate to measurements by obeying
82 fundamental physical constraints (Berliner, 2003; Lowman and Barros, 2014). In this manuscript,
83 we propose, and evaluate a general physical-statistical framework to retrieve SWE from SnowSAR
84 measurements across a heterogeneous landscape during SnowEx'17.

85

86 **2. Previous Work**

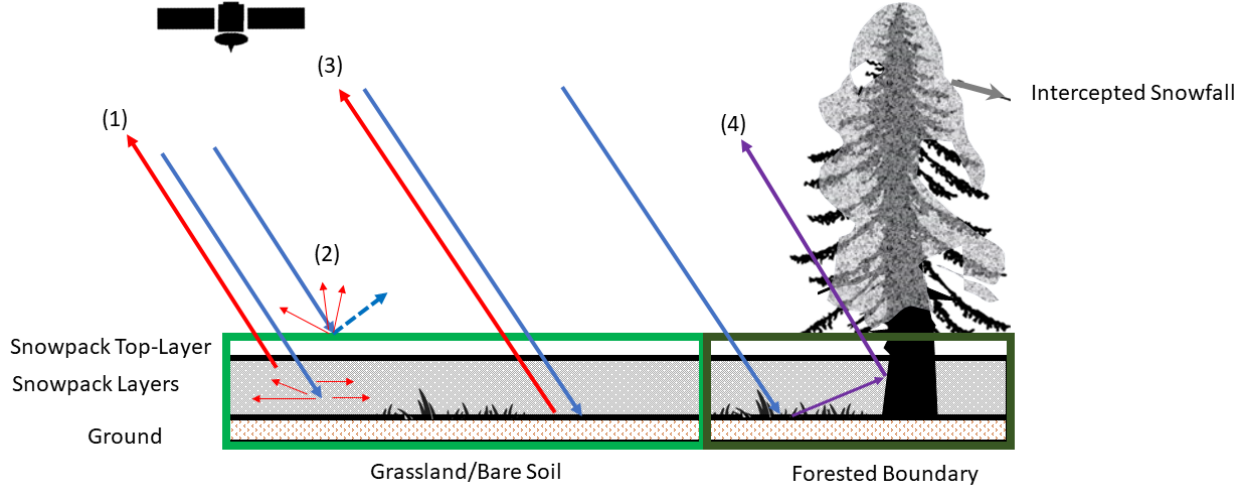
87 **2.1 Forward Simulation - From SWE to Backscatter**

88 The advantage of SAR technology is the high-spatial resolution of its measurements, which is
89 necessary to capture the spatial heterogeneity of snowpack physical processes (e.g. Deems et al.
90 2016; Mendoza et al., 2020; Manickam and Barros, 2020) as demonstrated in forward simulations.
91 Cao and Barros (2020, 2023a; hereafter CB20 and CB23) demonstrated the utility of a multi-layer
92 snow hydrology (MSHM) coupled with a radiative transfer model (RTM) forced by high-
93 resolution operational numerical weather prediction (NWP) model forecasts to capture the
94 seasonal hysteresis behavior of the seasonal snowpack at Grand Mesa and Senator Beck in
95 Colorado against Sentinel-1 C-band measurements.

96 The MSHM is a physically driven snow hydrology model that simulates the evolution of snowpack
97 physical properties including detailed stratigraphy (Kang and Barros, 2012a-b; CB20). During
98 snowfall events, fresh snow is added to the top layer of the snowpack until a threshold
99 accumulation is met, and a new layer forms. The RTM used here is MEMLS3a (Microwave
100 Emission Model of Layered Snowpacks adapted to include backscattering by Proksch et al., 2015).
101 MEMLS is a physically driven radiative transfer model which takes snowpack characteristics as
102 inputs and simulates its microwave emission for a frequency band with four polarizations – HH,
103 VV, HV and VH (originally proposed by Wiesmann and Mätzler, 1999). To estimate total
104 scattering, ground backscatter σ_{bkg} must be modeled as well, as described below. .

105 Figure 1 illustrates the various backscatter mechanisms contributing to total backscatter (σ_{total}) in
106 active microwave measurements represented in MEMLS3&a, the RTM: volume backscatter (σ_{vol})
107 from the multiple interactions of the incoming radar signal within the snowpack, the backscatter
108 at the snowpack-air interface (σ_{surf}) and at the snowpack-ground interface including interactions
109 with submerged vegetation and litter (σ_{bkg}). In forested areas, additional backscatter mechanisms
110 are associated with the multiple bounce pathways among tree canopy, intercepted snow, tree
111 trunks, and snowpack. Depending on viewing geometry (flight path and incidence angle), σ_{total}
112 measurements from areas without trees in regions of mixed landcover can include significant
113 contribution from trees along the grassland-forest transitions.

114



115

116 **Figure 1:** Scattering mechanisms for grassland submerged by snow and snowpack over bare soil or rock: (1) Volume Backscatter
 117 σ_{vol} ; (2) surface backscatter σ_{surf} ; (3) background backscatter at the snow-ground interface σ_{bkg} ; (4) snowpack-ground-canopy-tree
 118 trunk interactions at forested boundaries. Red arrows (1), (2) and (3) are resolved in the retrieval applications demonstrated here.

119

120 CB23 used the coupled MSHM-MEMLS in forward mode to predict Sentinel-1 C-band volume
 121 backscatter σ_{vol} without calibration or nudging of ground observations without bias and within \pm
 122 2.5 dB at 90 m resolution across terrain slopes in the $[10^\circ-52^\circ]$ range for barren land, alpine grass
 123 and shrubs and in forested areas with snow-free canopy at the beginning of spring in the Senator
 124 Beck Basin in Colorado. They estimated σ_{bkg} as the average of Sentinel-1 measurements for
 125 snow-free conditions. Cao and Barros (2023b) modified MEMLS3&a to include double-bounce
 126 effects among snowpack and vegetation (MEMLS-V) and retrieved σ_{bkg} from total backscatter
 127 σ_{total} measurements in mixed landcover using simulated annealing. Their estimates are consistent
 128 with CB23, suggesting potential to simplify the inverse-problem of estimating snowpack physical
 129 properties from total backscatter measurements in mixed landcover and further simplify the
 130 physical-statistical retrieval framework proposed here, although further evaluation is necessary.

131

132 2.2 Physical-Statistical Retrieval

133 For retrieval in a Bayesian framework, the probability of the retrieved geophysical variable x (the
 134 inferred posterior distribution) is conditional on the *a priori* knowledge of the variable x (the prior
 135 distribution), indirect measurements D , and a physical model $M(\eta)$ (e.g., the snow radiative
 136 transfer algorithm in this case) with physical parameters η (including x) and statistical error
 137 parameters ζ . The joint probability distribution of M , D , η , and ζ can be written as:

$$138 \quad P(M, D, \eta, \zeta) = P(D|M, \eta, \zeta) \times P(M|\eta, \zeta) \times P(\eta, \zeta) \quad (1)$$

139 The first term to the right-hand side of Eq. (1) is the backscatter data model, the second term is the
 140 prior of the backscatter, and the third term is the prior of the snowpack physical parameters
 141 (including snow depth and snow density, etc) with statistical error parameters. Assuming the

142 measurements do not depend on the physical parameters, the model does not depend on the
 143 statistical error parameters, and that the physical parameters and the statistical parameters are
 144 independent, Eq. (1) can be revised to read

$$145 \quad P(M, D, \eta, \zeta) = P(D|M, \eta) \times P(M|\eta) \times P(\eta) \times P(\zeta) \quad (2)$$

146 And finally in the context of specific measurements y with known uncertainty described by $P(y)$

$$147 \quad P(M, \eta, \zeta | y) = P(y|M, \eta) \times P(M|\eta) \times \frac{P(\eta) \times P(\zeta)}{P(y)} \quad (3)$$

150 The physical model M and $P(y)$ are invariant and assuming that we have a good understanding of
 151 the statistical errors, then Eq. (3) can be further simplified as follows

$$152 \quad P(\eta|y) \propto P(y|\eta) \times P(\eta) \quad (4)$$

153
 154 In the context of Bayesian inference the goal is to maximize $P(\eta|y)$, the posterior probability of
 155 physical parameters conditional on measurements informed by the a priori parameter probabilities
 156 $P(\eta)$. This implies maximizing the second term in Eq.(4), the posterior of the backscatter
 157 conditional on physical parameters η , implies minimizing the difference between measurements y
 158 with known error covariance matrix Σ_y and model predictions $M(\eta)$. For multiple concurrent
 159 measurements, $P(y|\eta)$ can be described by a multivariate normal distribution,

$$160 \quad P(y|\eta) = (2\pi)^{\left(-\frac{N}{2}\right)} |\Sigma_y|^{-\frac{1}{2}} \exp\left[-\frac{1}{2}(y - M(\eta))^T \Sigma_y^{-1} (y - M(\eta))\right] \quad (5)$$

161 where N is the number of measurements at a given location and time (e.g. backscatter at different
 162 frequencies as in Durand and Liu, (2012).

163 Pan et al. (2023, hereafter P23) adapted a Bayesian retrieval algorithm previously developed to
 164 estimate SWE from passive microwave measurements (Pan et al. 2017, hereafter P17) to active
 165 microwave, hereafter referred to as Base-AM. The snow radiative transfer algorithm in Base-AM
 166 is MEMLS, and the semi-empirical Dobson model is used to estimate the soil dielectric constant
 167 as a function of soil moisture and soil texture (Dobson et al. 1985; Hallikainen et al. 1985). A
 168 Monte Carlo Markov Chain (MCMC) iterative algorithm (Metropolis et al. 1953) is used to sample
 169 from $P(\eta|y)$ starting from initial values and using the likelihood ratio criteria to achieve
 170 convergence. In this work, realistic snowpack predictions from MSHM-MEMLS are used to
 171 define the prior distributions of parameters and constrain the Bayesian retrievals: y represents the
 172 SnowSAR backscatter measurements and η represents to all model parameters and geophysical
 173 variables including SWE, SD, snow density.

174

175 **3. Study Area and Data**

176 **3.1 Study Area and Ancillary Data**

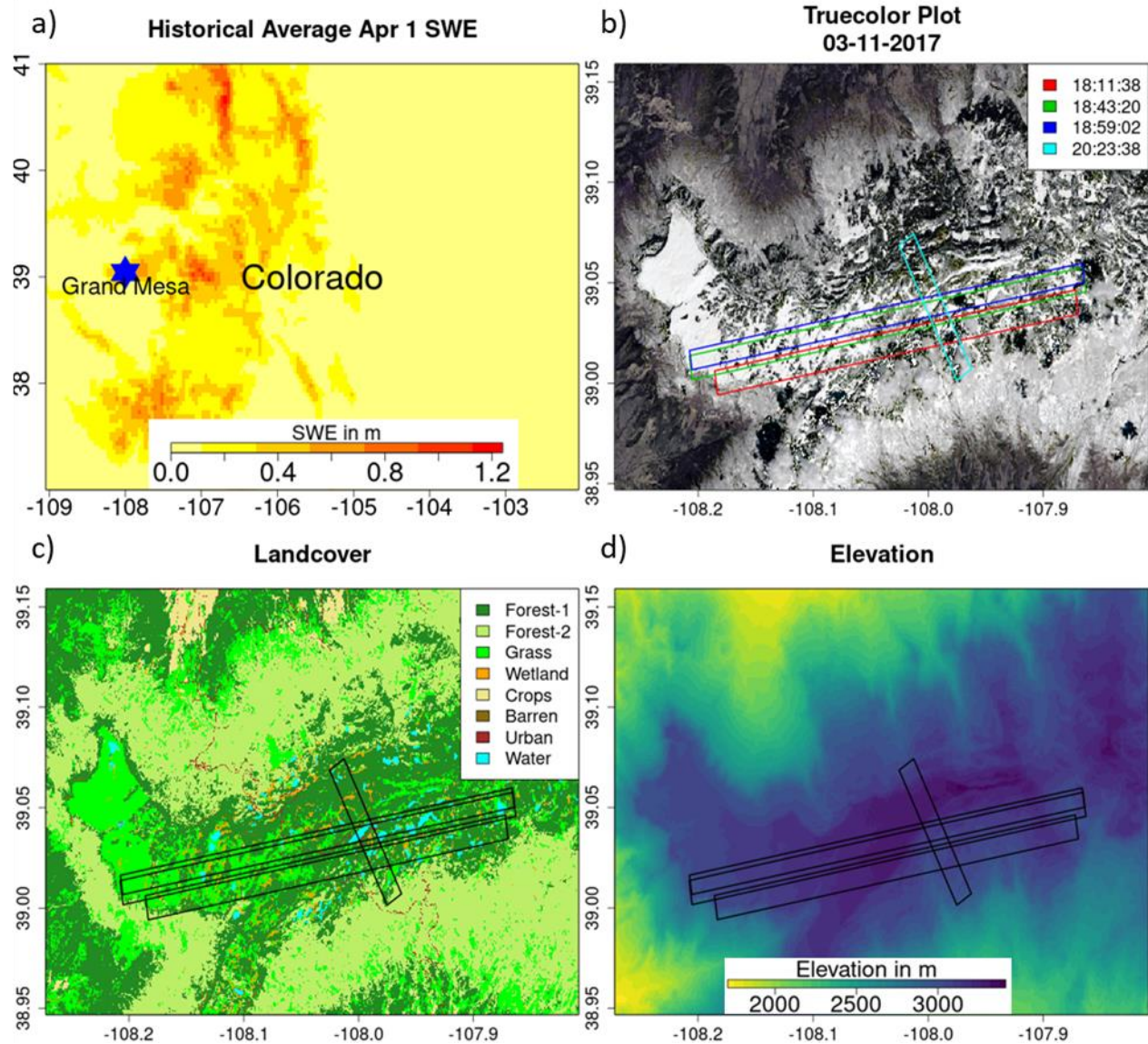
177 The study region is Grand Mesa, Colorado, a plateau that is 2,000 m above adjacent low-lying
 178 areas and is surrounded by ridges up to 500m in elevation (as depicted in Fig. 2). Grand Mesa
 179 has an alpine climate, experiencing snowfall throughout the year except during the months of July
 180 and August. Landcover is heterogeneous with grasslands in the west and a mix of evergreen and
 181 deciduous forest to the east. Numerous wetlands are widespread across the Mesa, especially in the
 182 transition from grassland to forest. The land cover data were obtained from the National Land Data
 183 Assimilation System (NLDAS). The datasets were upscaled to 90 m using nearest neighbor
 184 interpolation to support retrievals at 90 m resolution (see Section 4). NLDAS is used to determine
 185 landcover type in the snow hydrology model. NALCMS is used to upscale the evaluation data.
 186 Hourly albedo is derived from NLDAS at 12.5 km resolution. A summary of all the datasets used
 187 in this study is available in Table 1.

188

189 **Table 1:** Summary list of datasets used in the study.

Data	Source	Spatial Resolution		Temporal Resolution		Date Range	Relevant Link
		Initial	Final	Initial	Final		
Rainfall Temperature Air Pressure Incoming SW radiation Incoming Longwave radiation Wind speed Humidity	HRRR	3 km	30 m, 90 m	1 hr	30 min	9/1/2016 - 2/25/2017	https://rapidrefresh.noaa.gov/hrrr/
Albedo	NLDAS	12.5 km	30 m	1 hr	30 min	9/1/2016-2/25/2017	https://ldas.gsfc.nasa.gov/
Backscatter	SnowSAR – SnowEx’17	1 m	30 m, 90 m	-	-	2/21/2017	https://nsidc.org/data/snex17_snowsar/versions/1
Landcover	NLCD, NALCMS	30 m	30 m, 90 m	-	-	-	https://www.usgs.gov/centers/eros/science/national-land-cover-database http://www.cec.org/north-american-land-change-monitoring-system/
Snow Depth	LIDAR – SnowEx’17	3 m	30 m, 90 m	-	-	2/25/2017	https://nsidc.org/data/aso_3m_sd/versions/1
SWE	Snowpit – SnowEx’17	-	-	-	-	2/20/2017-2/24/2017	https://nsidc.org/data/snex17_snowpits/versions/1

190



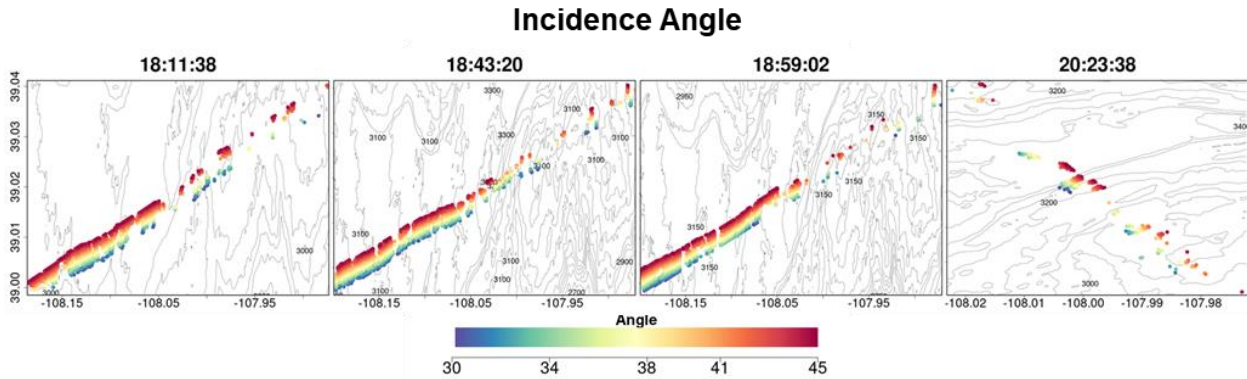
191
 192 **Figure 2:** Study area in Grand Mesa, Colorado. a) Location of Grand Mesa in Colorado, with historical Apr 1 SWE average as
 193 base map. b) Paths of 4 SnowSAR SnowEx'17 flights on 21 Feb 2017, with true color image obtained from Landsat on 03/11/2017
 194 as the base map. c) Land cover of the study region. Forest-1 are needle leaf forests; Forest-2 are broadleaf forests. d) Digital
 195 elevation map of the study region.

196

197 3.2 Atmospheric Forcing

198 Numerical Weather Prediction (NWP) outputs are used as the atmospheric forcing for the snow
 199 hydrology model and to set up boundary conditions. Previously, CB20 and CB23 relied on HRRR
 200 (High-Resolution Rapid Refresh) hourly forecasts at 3 km and downscaled it to 90 m in Grand
 201 Mesa. Here, the same data set was independently downscaled to 30 m as well. The HRRR dataset
 202 is produced by National Ocean and Atmospheric Agency (NOAA) by hourly assimilation of
 203 observations at 13 km resolution (Benjamin et al., 2016; Table 1). Hourly atmospheric forcing
 204 was linearly interpolated to 30 min temporal resolution used in the snow hydrology model.

205



206

207 **Figure 3:** Maps of incidence angles along SnowSAR flight paths on February 21, 2017 during SnowEx'17.

208

209 3.3 SnowSAR Backscatter

210 During SnowEx'17, airborne microwave backscatter measurements were made in Grand Mesa on
211 21 Feb 2017 at 1 m resolution (Table 1). The SnowSAR instrument is a dual frequency (X and Ku
212 Band) radar. A total of six flightlines were completed, two short ones on sloped densely forested
213 terrain and four long lines on the plateau. Here, only the four flightlines on the plateau are used for
214 analysis (Fig. 2 and Fig. 3). The flights are between 18:00 and 21:00 GMT (noon – 3PM MST).
215 SnowSAR data quality control measures included filtering based on aircraft attitude (there were
216 line segments with turbulence), beam incidence angle/antenna pattern, and signal-to-noise-ratio of
217 the backscatter coefficients. Processing of the original airborne SAR measurements and quality
218 control indicate that only the co-pol X-band HH- and VV-pol as well as Ku-band VV-pol
219 measurements are adequate for retrieval. Geolocation was verified against corner reflector targets
220 and geographic features and found to be very robust. The SnowSAR data were upscaled to 30 m
221 and 90 m resolution by simple averaging of all SnowSAR measurements within each pixel.

222

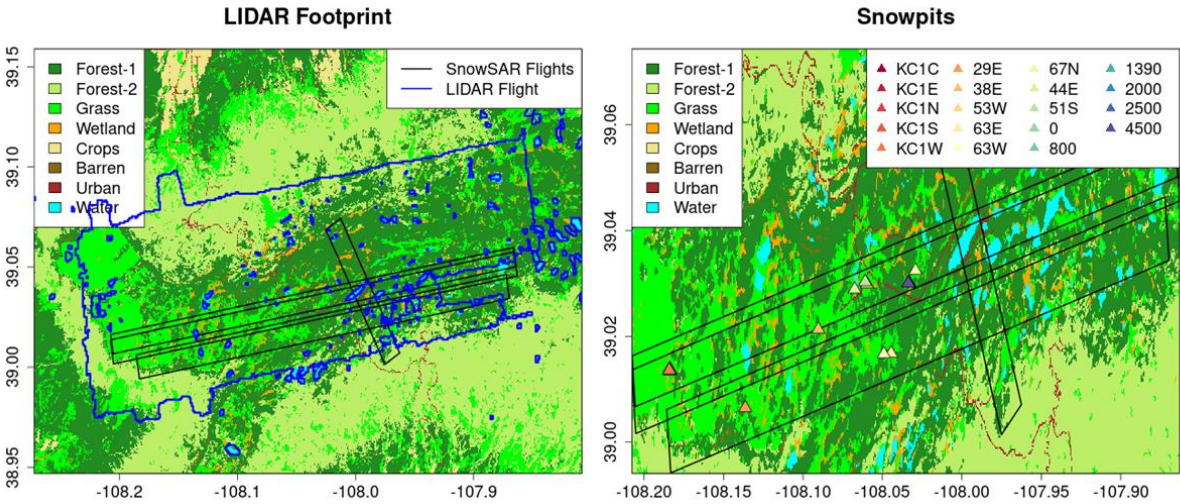
223 3.4 Validation Data

224 *LIDAR Snow Depth* – The Airborne Snow Observatory (ASO) LIDAR measurements of snow
225 depth at 3m resolution across Grand Mesa are available for SnowEx'17 on February 25, thus 4
226 days after the SnowSAR flights (Painter et al., 2018; Table 1). There were no significant snow
227 storms or strong winds in that period, except for about 3mm of rainfall for less than 1 hour on
228 February 24. These data are used to examine the distribution of retrieved snow depths, that is
229 indicative of the spatial heterogeneity of the snowpack, and the relative absolute differences
230 between LIDAR measurements and retrieval of snow depth, that are indicative of local retrieval
231 errors. The LIDAR data were upscaled to 30 m and 90 m using simple averaging (e.g., Fig.4a).
232 There can be large snow depth underestimation errors associated with upscaled LIDAR retrievals
233 along the edges of forests where the snow depth is underestimated consistent with previous work
234 (e.g. Deems et al. 2013; Jacobs et al. 2021). Given the expected measurement uncertainty on the

235 order of 10-20 cm in Grand Mesa, which is amplified by microtopography, LIDAR pixels with
236 snow depth shallower than 20 cm are not considered for evaluation.

237 *Snowpit SWE* - Multiple snowpits were excavated during the SnowEx'17 field campaign across
238 Grand Mesa (Table 1). Due to the small number of snow pit measurements along the SnowSAR
239 flightlines on 21 February, snowpit measurements on 20-24 of February were considered for
240 evaluation assuming that in the absence of snowstorms or other weather events the snow pack
241 does not change significantly during the 4-day period. Differences are expected at local places but
242 the overall spatial trends should be maintained such as the west-east gradient in snow depth. The
243 values of snowpit SWE are estimated using an average of the snow density measurements at
244 different depths applied to the entire snow depth. Only pits in the non-forested areas were selected
245 for evaluation (Fig. 4b).

246



247
248 **Figure 4:** a) Flight footprint of the LIDAR instrument used to measure the snow depth during SnowEx'17. b) Location of snow
249 pits used to measure SWE 20-24 Feb 2017. The legend identifies SnowEx'17 Pit IDs.

250

251 4. Retrieval Algorithm

252 Simplicity and computational efficiency are desirable attributes for an operational algorithm that
253 produces successful retrievals, here understood as meeting science uncertainty requirements and
254 latency adequate to meet applications needs defined by NASEM (2018). The retrieval
255 methodology builds on existing and well evaluated snow hydrology, radiative transfer, and
256 physical-statistical models (CB20,CB23, P17, P23) previously reviewed in Section 2. A list of
257 forcings and coupling variables and parameters among MSHM, MEMLS and Base-AM is
258 provided in Table 2.

259 Averaging is necessary to reduce the signal to noise ratio (SNR) in SnowSAR measurements at
260 their native resolution (Section 3.3). Because the highest spatial resolution of available ancillary
261 data sets is 30 m, the SnowSAR measurements were upscaled to 30 m to eliminate the need for

262 interpolation and, or downscaling that introduce further uncertainty. Following results by
 263 Manickam and Barros (2020), the algorithm was also applied at 90 m resolution consistent with
 264 the first scaling break identified in Sentinel-1 SAR backscatter. The implication of linear scaling
 265 behavior is that successful retrievals at 90 m resolution can subsequently be statistically downscaled
 266 with confidence, which has significant computational advantages. Further upscaling was not
 267 conducted because the number of pixels becomes very small given the available coverage of
 268 SnowSAR flights.

269

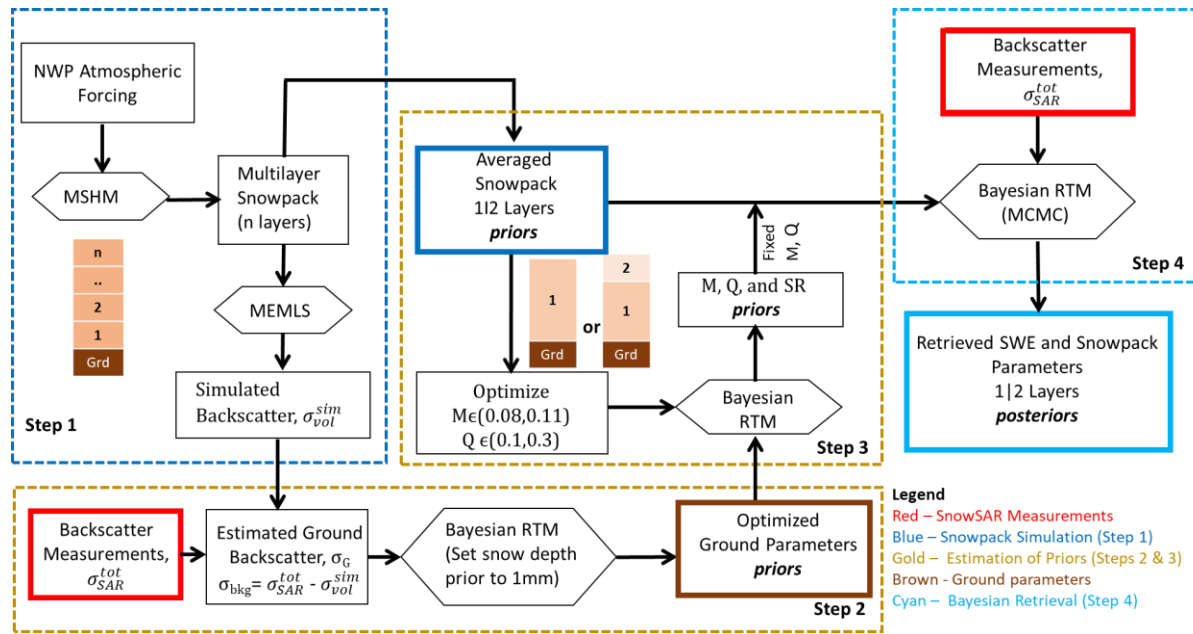
270 **Table 2:** Input and output parameters from the three models in the SWE physical-statistical retrieval framework.

Model	Input	Output	Reference
MSHM	Rainfall Temperature Air Pressure Incoming shortwave radiation Incoming longwave radiation Wind speed Humidity Albedo	Snow Temperature Profile Soil Temperature Profile Snow Density Profile Snow Depth Layering Profile Liquid Water Content Profile Snow Correlation Length Profile	Cao and Barros (2020)
MEMLS	Snow Temperature Profile Soil Temperature Profile Snow Density Profile Snow Depth Layering Profile Snow Correlation Length Profile Cross polarization fraction Ground rms height	Diffused Reflectivity Profile Specular Reflectivity Profile Total Backscatter Coefficient	Proksch et al. (2015)
Base-AM	Equivalent Snow Temperature Prior Equivalent Soil Temperature Prior Equivalent Snow Density Prior Equivalent Snow Depth Prior Correlation Length Cross polarization fraction Ground rms height Total Backscatter Coefficient Prior	Optimized – Snow Layer Depth Snow Density	Pan et al., (2023)

271

272 Figure 5 illustrates the retrieval workflow consisting of four main steps. **Step 1** - Snow hydrology
 273 simulation using MSHM to produce a layered snowpack and volume backscatter simulation using
 274 MEMLS (σ_{vol}^{sim}). **Step 2** - Bayesian estimation of ground parameter priors that govern background
 275 backscatter σ_{bkg} using MEMLS assuming a very thin film of snow on the ground (1 mm SD) at the
 276 beginning of the accumulation season and estimation of the σ_{bkg} by subtraction of σ_{vol}^{sim} from
 277 SnowSAR total backscatter measurements σ_{SAR}^{tot} . **Step 3** - Determination of snowpack priors for
 278 Bayesian SWE retrieval using results Step 1 and Step 2. **Step 4** - Bayesian optimization of
 279 simulated σ_{SAR}^{tot} to derive posterior distributions of SD and ρ_{snow} for the single- and two-layer (1|2)
 280 equivalent snowpack, and subsequent calculation of retrieved SWE posterior distributions

281



282

283 **Figure 5:** Workflow of the SWE Physical-Statistical retrieval framework. NWP atmospheric forcings drive MSHM to determine
 284 priors for the Bayesian radiative transfer model (Base-AM) and synthetic backscatter for ground parameters. SnowSAR backscatter
 285 measurements are assimilated to determine the posterior distribution of the snowpack parameters.

286

287 4.1 Layered Snowpack Simulations (Step 1)

288 Following the methodology presented in Section 2.1, MSHM was run for a full-year starting from
 289 snow free conditions on September 1st 2016 using downscaled HRRR data as atmospheric forcing
 290 (Section 3.2) and a timestep of 30 mins. On the day of the SnowSAR flights, the snowpack
 291 physical properties predicted at times corresponding to each of the four flights are used to derive
 292 the 1|2 Layer equivalent snowpack properties used in the retrieval. The simulated volume
 293 backscatter (σ_{vol}^{sim}) was estimated by specifying the cross polarization fraction parameter $Q=0.2$
 294 following CB20. This is an empirical coefficient that distributes the diffuse scattering into cross
 295 and like polarization components in MEMLS (Proksch et al. 2014).

296 In realistic layered snowpacks, stratigraphy (i.e., vertical heterogeneity) is a dominant feature of
 297 the density, temperature, microstructure, and dielectric properties (e.g., emissivity and
 298 reflectivity). The vertical structure of snow microstructure in MSHM is described using a
 299 parameterization of snow correlation length (l_{ex}) consistent with MEMLS formulation. Depending
 300 on the number of layers, this poses an undetermined problem as the number of measurements is
 301 equal to the number of frequencies and the number of polarizations available (typically two or
 302 three). For example, there are only four observations for a dual-frequency measurement with dual
 303 polarization. In contrast, the set of independent parameters per layer includes snow density, layer
 304 thickness, liquid water content, snow grain size or correlation length, temperature, reflectivity, and
 305 transmissivity.

306 While converting the multi-layer snowpack to a single-layer model is the simpler path to address
 307 the undetermined inverse-problem, fresh snowfall accumulation and snowpack crusting artifacts

308 due to melt-refreeze cycles, as well as hardening by wind action introduce strong density and grain
 309 size differences at the top of the snowpack. To capture this behavior, we implement and evaluate
 310 the retrieval algorithm for both single and two-layer equivalent snowpacks derived from the
 311 layered snowpack simulated by MSHM. The equivalent single- or two-layered snowpack
 312 parameters for each pixel are obtained by matching SWE, snow depth (SD) and volume backscatter
 313 (σ_{vol}^{sim}) of the simulated multilayer snowpack.

314

315 4.2 Ground and Snowpack Parameter Priors (Steps 2 and 3)

316 A first estimate of the σ_{bkg} is obtained by subtracting σ_{vol}^{sim} from SnowSAR X-band HH-pol
 317 σ_{SAR}^{tot} measurements following Baghdadi et al. (2011) who found better performance among
 318 backscattering models for HH-pol against TerraSAR-X measurements. In Base-AM, σ_{bkg} depends
 319 on the effective effective soil moisture and soil surface roughness. To optimize these parameters,
 320 σ_{bkg} is used as an “observed” value. To simulate snow-free conditions the snow depth is
 321 constrained to a maximum value of 1 mm in Step 2. The cross polarization fraction Q initially
 322 specified as Q=0.2 is optimized first and separately from other ground parameters in the third step
 323 of the retrieval algorithm (Fig. 5). The posterior distributions of the ground parameters in Step 2
 324 are used along with the 1|2 layer prior distributions and the SnowSAR measurements to estimate
 325 the posterior distributions of snow depth and snow density using the Base-AM framework (Fig. 5)
 326 and both X- and Ku-band VVpol. SWE is subsequently derived from snow depth and snow density.

327 *Single-layer Snowpack* - The total snow depth and the averages of multilayered snowpack
 328 parameters are specified as the mean of the prior distribution for retrieval. Table 3 shows the range
 329 and standard deviation of the parameters.

330

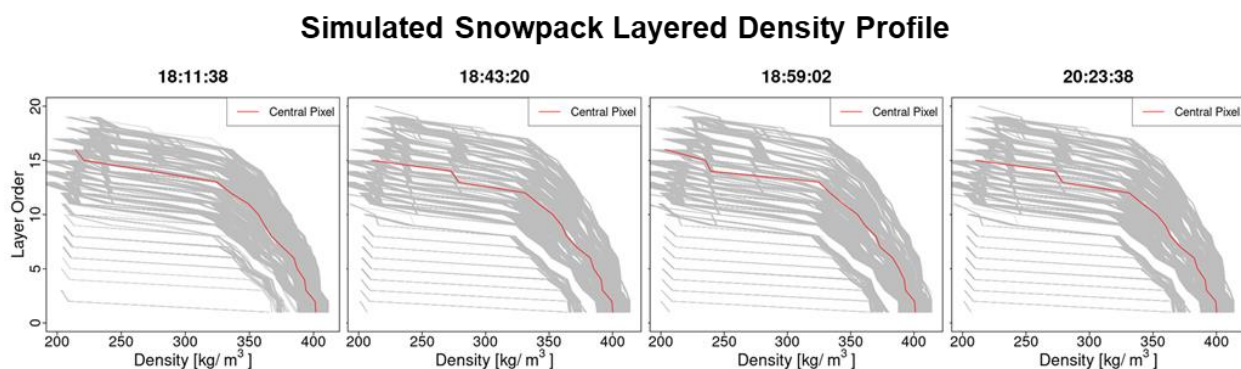
331 **Table 3:** Base-AM model input variance and range for the parameters prepared using MSHM multilayer snowpack parameters.
 332 Alphanumerical subscript in 2-layer snowpack retrievals denotes layer number: 1- bottom layer; 2- top layer; avg- the average of
 333 all MSHM multilayer parameter values in the corresponding single or 2-layer snowpack. DZ is the MSHM snow depth.

Snow Parameters	1 Layer Snowpack			2 Layer Snowpack			
	Variance, σ^2	Range		Variance, σ^2		Range for each layer	
		Min	Max	Bottom	Top	Min	Max
Snow Temp., Ts [$^{\circ}$ C]	$0.3 \times Ts_{avg}$	$1.3 \times Ts_{min}$	$0.7 \times Ts_{max}$	$0.3 \times Ts_{1,avg}$	$0.3 \times Ts_{2,avg}$	$1.3 \times Ts_{min}$	$0.7 \times Ts_{max}$
Snow Density, ρ [Kg/m ³]	$0.3 \times \rho_{avg}$	$0.8 \times \rho_{min}$	$1.2 \times \rho_{max}$	$0.3 \times \rho_{1,avg}$	$0.3 \times \rho_{2,avg}$	$0.8 \times \rho_{min}$	$1.2 \times \rho_{max}$
Snow Depth, DZ [m]	$0.3 \times DZ$	$0.5 \times DZ$	$1.5 \times DZ$	$0.1 \times DZ_1$	$0.2 \times DZ_2$	$0.2 \times DZ$	$0.9 \times DZ$
Correlation Length, l_{ex}	$0.3 \times l_{ex,avg}$	$l_{ex,min}$	$l_{ex,max}$	$0.2 \times l_{ex,1,avg}$	$0.2 \times l_{ex,2,avg}$	$l_{ex,min}$	$l_{ex,max}$
Soil Temp., Tsoil [$^{\circ}$ C]	0.3	1.3		0.3		1.3	

334

335 *Two-layer Snowpack* – The average values of the snowpack physical properties for each layer are
 336 derived from the multilayer snowpack simulated by MSHM. The key requirement is to determine
 337 the depth of each one of the layers that best captures the snowpack vertical structure. Figure 6
 338 shows MSHM simulated snowpack density profiles for each of the four SnowSAR flights. The
 339 shape of the profiles reflects the interplay between thermodynamic processes that change snow
 340 microstructure and dominate in the upper snowpack and mechanical consolidation processes that
 341 are dominant in the mid and lower layers. The snow depth point corresponding to the maximum
 342 change in snow density between adjacent layers in the multilayer snowpack is used here to divide
 343 the snowpack in two layers. Subsequently, the layer-depth weighted average density, snow
 344 temperature, and correlation length of the MSHM multilayer snowpack is calculated for the
 345 corresponding depths of the two-layer equivalent snowpack (Table 3).

346



347

348 **Figure 6** - Density profiles simulated by MSHM for all grassland pixels at 30 m resolution from the 4 SnowSAR flight paths. The
 349 density profile of the central pixel for each of the flights is marked in red. The snowpack layers are numbered from bottom to top
 350 tracking the evolution of simulated snowpack stratigraphy during the accumulation season. Note the significant difference between
 351 the top 2-3 layers and the deeper snowpack supporting the two-layer snowpack conceptual retrieval model.

353

354 **4.3 Bayesian Optimization (Step 4)**

355 Realistic snowpack predictions from MSHM driven by weather forecasts (Step 1) are used to
 356 define the prior distributions of snowpack parameters and constrain Base-AM (Steps 2 and 3) to
 357 infer the posterior distribution of snowpack parameters given the SnowSAR backscatter
 358 measurements (Step 4) as discussed in Section 2.2.

359 The local mean of the posterior distribution for each parameter is hereafter referred to as the
 360 retrieval result for each pixel. SD retrievals are evaluated against LIDAR snow depth including
 361 spatial patterns and gradients, and overall statistical structure using histograms. SWE retrievals
 362 derived from the posterior distributions of snow density and snow depth are evaluated against SWE
 363 measurements at snowpits (Section 3.4). Original LIDAR measurements were reprojected and
 364 coregistered with the SnowSAR retrievals. A comparative analysis was conducted to examine the
 365 dependence of retrievals on incidence angle and the subgrid scale variability was quantified in
 366 terms of the standard deviation of original LIDAR measurements within the upscaled pixel. The

367 amplitude error metrics are the mean, standard deviation, and mean absolute relative error
368 (MARE):

$$369 \quad MARE = \frac{\sum_{i=1}^n |1 - R_i/O_i|}{N} \quad (6)$$

370 where O are observations and R are retrievals. The Bhattacharya coefficient (BC) is used to
371 compare the spatial distributions of snow depth and backscatter. BC measures the similarity
372 between two probability distributions p_1 and p_2 as follows (Bhattacharya, 1943)

$$373 \quad BC = \sum_{i=1}^N \sqrt{p_1(i)p_2(i)} \quad (7)$$

375 Finally, among the 39 snowpits available for evaluation on February 21, only 15 pits in open areas
376 (i.e. grasslands) were retained for evaluation and snow pits without SnowSAR measurements
377 within a radius of 100 m were discarded.

378

379 **5. Results and Discussion**

380 **5.1. Successful Retrievals**

381 SnowSAR measurements are strongly affected by aircraft operations, viewing geometry that varies
382 systematically along the flight path resulting in amplitude artifacts amplified by landform and
383 landcover heterogeneity. Even after separating homogeneous grassland pixels, there is
384 contamination from multiple bounce artifacts at grassland-forest transitions and adjacent wetlands
385 that cannot be resolved at 30 or 90 m resolution. Other errors embedded in the retrieval are
386 associated with downscaling of HRRR forcings that produce biased snow priors, snow hydrology
387 model structure, and errors tied to the background backscatter estimation. Combined these errors
388 compounded can lead to a weak convergence of the Bayesian optimization algorithm resulting in
389 large backscatter residuals. To account for these errors and meet NASEM (2018) science
390 requirements, SnowSAR pixels for which the relative residual backscatter (RRB) between Base-
391 AM simulated σ_{sim}^{tot} and SnowSAR measurements σ_{SAR}^{tot} was greater than 30% were identified as
392 unsuccessful. In an operational context, these pixels would be flagged and identified as failed or
393 highly uncertain retrievals. The successful retrieval fraction after restricting the range of incidence
394 angles and imposing the $RRB < 30\%$ criterion is summarized in Table 4 for the four flights, and
395 for both 1|2 layer snowpack retrievals at 30 and 90 m resolution. Except for the later flight path
396 over the predominantly forested areas in the eastern sector of Grand Mesa (Fig.1), the fraction of
397 successful retrievals by restricting the incidence angle and RRB varies between 75 and 87% across
398 the four SnowSAR flights with a maximum absolute bias of 1.2 dB. Only figures with retrieval
399 results at 30 m resolution are shown in the main text; retrieval results at 90 m resolution as well as
400 other supporting analysis can be found in Appendix A.

401

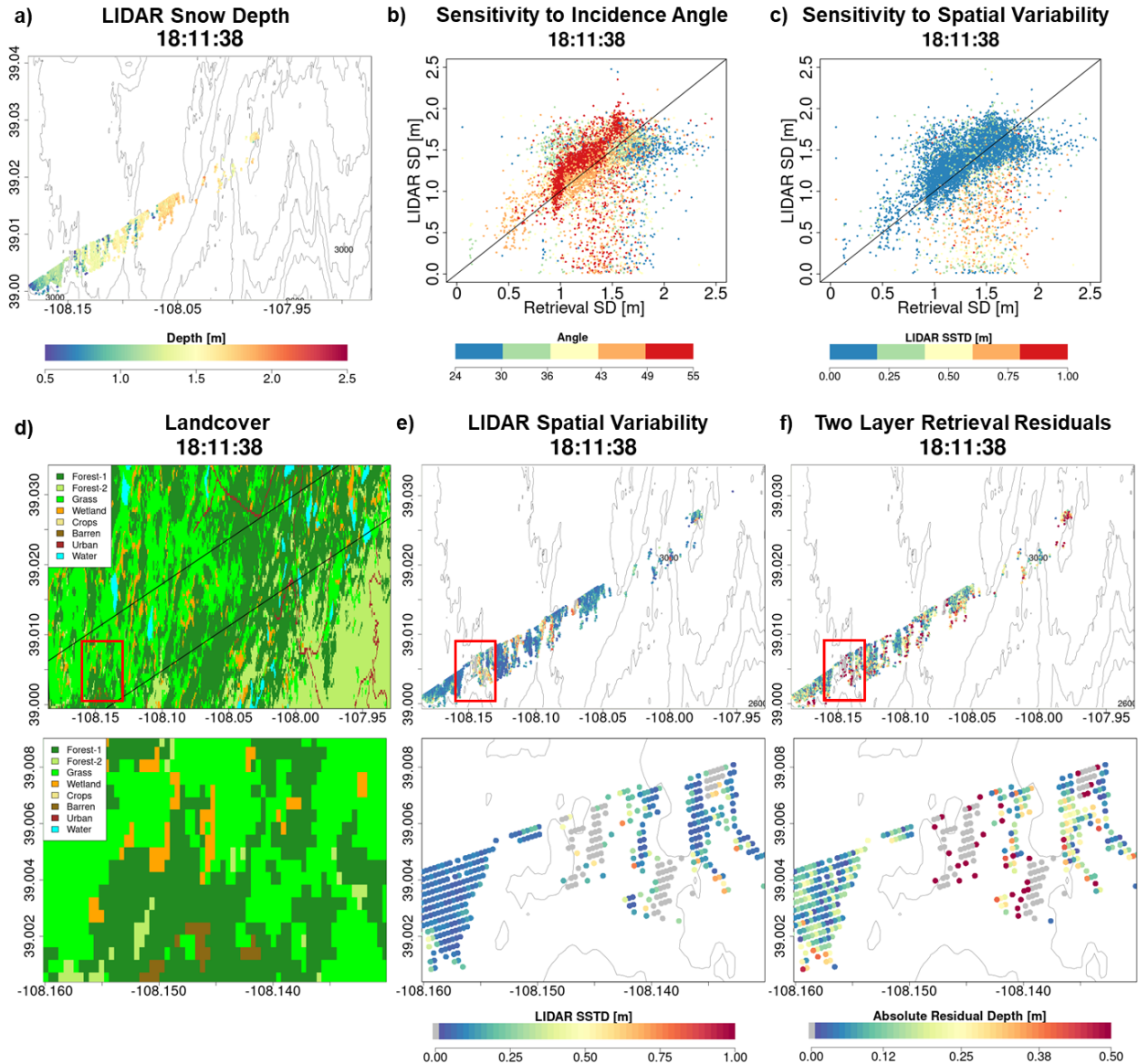
402 **Table 4:** Spatial bias between SnowSAR backscatter and converged backscatter from Base-AM for successful retrievals for
 403 grassland pixels at 30 and 90 m spatial resolution over each flight. Successful retrievals are for pixels with local incidence angles
 404 in the 30°-45° range and relative residual backscatter (RRB) of less than 30% for each of the four flights.

Flight Time	Successful Retrieval Fraction				Bias (Observed - Converged) [dB]							
	1 Layer		2 Layer		1 Layer				2 Layer			
	30 m	90 m	30 m	90 m	30 m		90 m		30 m		90 m	
					X	Ku	X	Ku	X	Ku	X	Ku
18:11:38	0.86	0.87	0.85	0.86	0.92	-0.45	0.96	-0.48	0.94	-0.46	0.97	-0.50
18:43:20	0.75	0.75	0.75	0.75	1.08	-0.54	0.98	-0.36	1.07	-0.46	0.98	-0.37
18:59:02	0.78	0.81	0.81	0.81	1.20	-0.78	1.21	-0.79	1.15	-0.73	1.22	-0.83
20:23:38	0.66	0.69	0.57	0.69	0.51	-0.58	0.70	-0.43	0.62	-0.85	0.72	-0.45

405

406 5.2. Retrieval Skill

407 Figure 7 compares LIDAR snow depth (Fig. 7a) against colocated SnowSAR retrievals at 30 m
 408 for the SNOWSAR flight at 18:11:38 GMT(GMT=MST+6). The SnowSAR retrievals for high
 409 incidence angles underestimate the LIDAR snow depth (orange and red points). Lemmetyinen et
 410 al. (2022) suggested a nominal incidence angle of 35°-45° for retrievals ensuring proper focusing
 411 and calibration of SnowSAR swaths. CB23 showed good skill in forward backscatter simulations
 412 for incidence angles as low as 30°. Overall the retrievals here also show very good performance
 413 for incidence angles between 30°-45°. Note however the large residuals for SnowSAR retrievals
 414 with high incidence angles (red and orange points in Fig. 7b) corresponding to LIDAR pixels with
 415 shallow snow depth (below the 1:1 line) and large subgrid-scale variability (orange and red points,
 416 Fig. 7c). Analysis for all flights at both 30 and 90 m resolution can be found in Appendix A (
 417 please see Figs. A1 and A2 similar to Fig. 7b; and Figs. A3 and A4 similar to Fig. 7c). Figures
 418 7d, 7e, and 7f show the landcover, spatial distribution of subgrid standard deviation (SSTD) and
 419 absolute residual (Retrieved – LIDAR) snow depth for the same flight. Along the edges of forest,
 420 the SSTD in the upscaled pixels is large due to high heterogeneity that cannot be resolved by the
 421 the LIDAR fusion algorithm for snow depth retrieval (Painter et al. 2016). The red box identifies
 422 an area with complex grassland-forest boundaries (Fig. 7d) and high subgrid scale variability (Fig.
 423 7e) resulting in poor LIDAR estimates. The edge of wetlands also has comparatively higher
 424 residuals than completely homogeneous grasslands. This corresponds to the LIDAR pixels with
 425 SSTD > 0.3 m (yellow, orange and red in Fig. 7c). Therefore, only LIDAR pixels with SSTD ≤
 426 0.3m are used for assessment of retrievals.



427

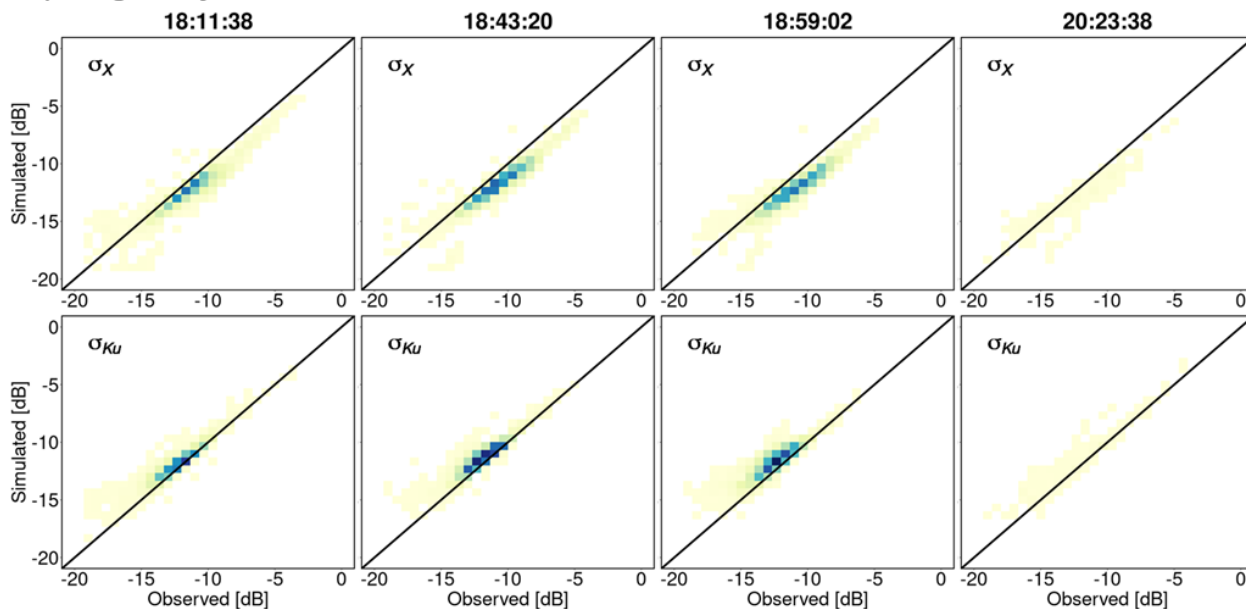
428 **Figure 7:** Snow depth measurements using airborne LIDAR on 2/25/17, 4 days after the SnowSAR flights. b) Comparison between
 429 LIDAR snow depth and the 2-layer retrieved snow depth from SnowSAR on 2/21/17 at 18:11:38 GMT. The pixels are color-coded
 430 according to the SnowSAR incidence angle. c) same as (b) with pixels color-coded according to the subgrid-scale variability
 431 measured by standard deviation of LIDAR snow depth within the corresponding 30 m pixel. Pixels on the edge of forests and
 432 grasslands have higher subgridscale standard deviations (SSTD). d) Landcover distribution along the flight path; bottom panel –
 433 zoom view of area in red box. e) Spatial distribution of upscaled LIDAR snow depth SSTD at 30m; bottom panel – zoom view of
 434 area in red box. The edges of forests have higher SSTD due to errors in the LIDAR snow depth retrievals at high resolution. f)
 435 Absolute residual between retrievals and LIDAR snow depth; bottom panel – zoom view of area in red box. Residuals equal to 0.5
 436 m and above are grouped in the same category. The red box in parts (d), (e), and (f) delineates an area with large absolute residuals.
 437 Vegetation-snowpack backscatter interactions at the grassland-forest and grassland-wetland margins not accounted for in the
 438 retrievals. Gray points in the central panel correspond to zero depth LIDAR estimates due to errors in heterogenous landcover..

439 Figure 8 shows heatmaps (density maps) to compare successful retrievals against observed X- and
 440 Ku-band VV-pol total backscatter at 30 m resolution. There is good agreement between the two
 441 values for both the bands specially in the -15 to -10 dB range without significant differences
 442 between single and two-layer snowpack retrievals. Note the positive bias in the case of X-band

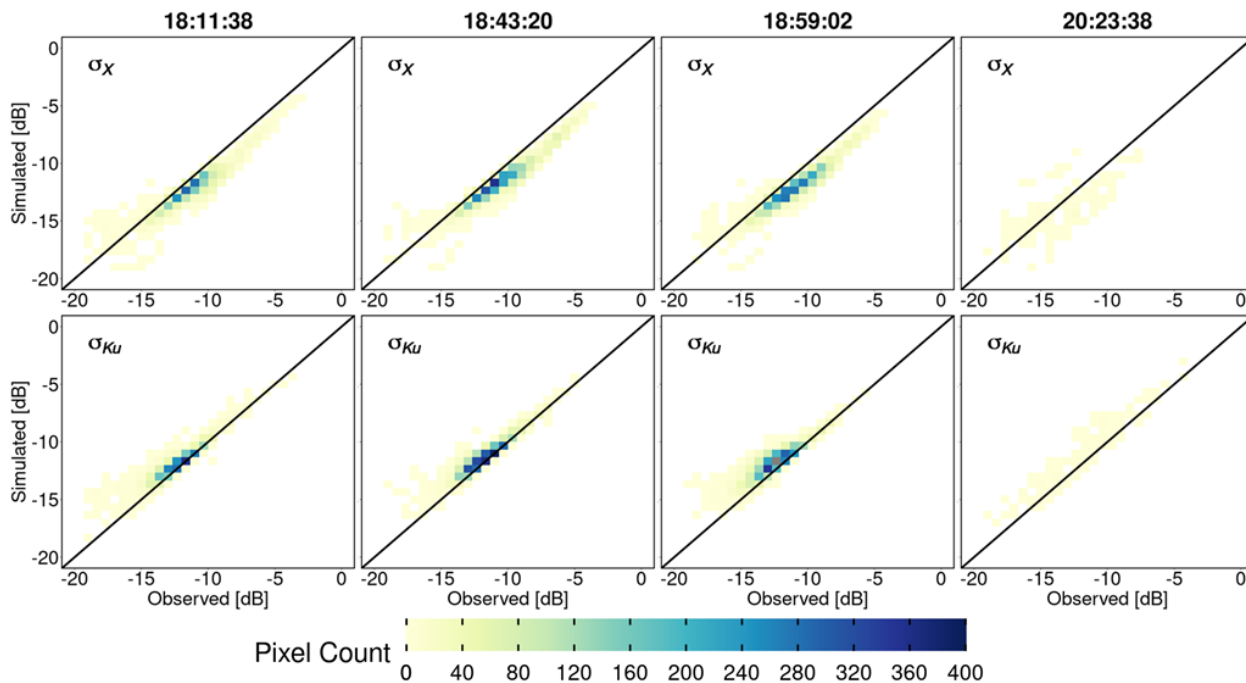
443 simulations compared to observations, whereas Ku-band has a negative bias as quantified in Table
 444 4. Overall, the retrievals at 90 m resolution show better agreement than those at 30 m resolution
 445 due to averaging (Fig. A5).

446

a) Single-Layer Retrievals



b) Two-Layer Retrievals



447

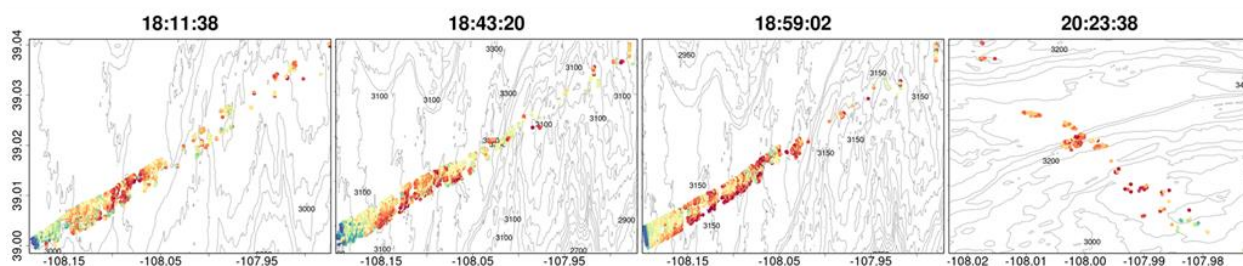
448 **Figure 8:** Heatmaps of SnowSAR measurements (observed) versus retrievals (simulated) backscatter (σ) at 30 m resolution for X-
 449 (σ_X) and Ku- (σ_{Ku}) bands: a) single-layer snowpack; and b) 2-layer snowpack. Successful retrievals are for pixels with local

450 incidence angles in the 30°- 45° range and relative residual backscatter (RRB) of less than 30% for each of the four flights (see
451 Table 4).

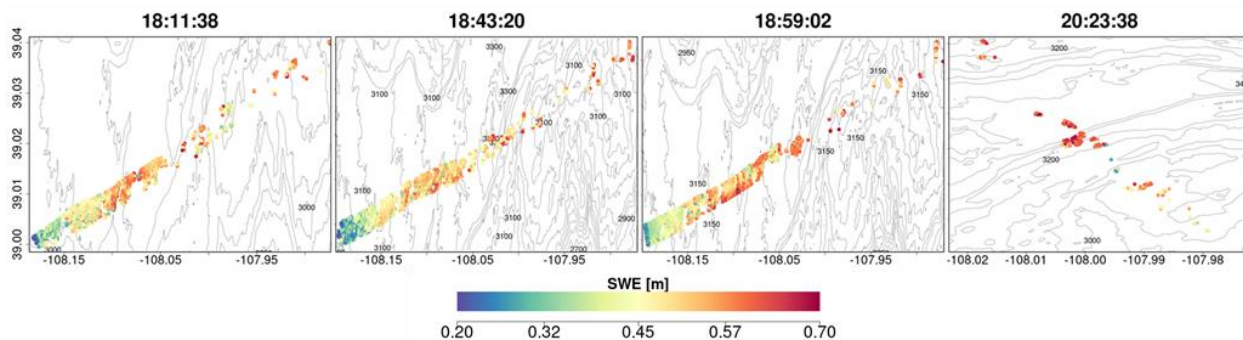
452
453 Maps of successful SWE retrievals for the four SnowSAR flight paths are shown in Fig. 9 and
454 Fig. A6 at 30 m and 90 m resolution, respectively. The retrievals capture well the west-east
455 gradient in SWE, and show realistic spatial variability across Grand Mesa. The very low SWE and
456 shallower snow depths at the easternmost boundary of the flightlines are underestimates
457 introduced by upscaling of the SNOWSAR backscatter values where there are significant changes
458 in topography at the edge of the Plateau (see Fig.2).

459

a) Single-Layer SWE Retrievals



b) Two-Layer SWE Retrievals

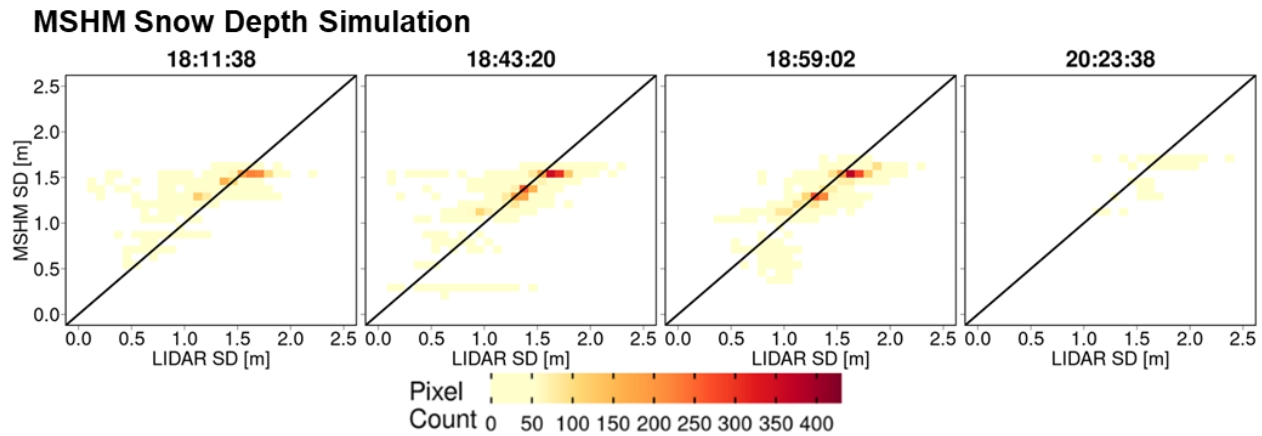


460
461 **Figure 9:** Spatial distribution of successful SWE retrievals for 1-layer (a) and 2-layer (b) snowpacks in grassland pixels at 30 m
462 resolution. Successful retrievals are for pixels with local incidence angles in the 30°- 45° range and relative residual backscatter
463 (RRB) of less than 30% for each of the four flights (see Table 4).

464
465 Heatmaps of total snow depth priors (MSHM predicted snow depth) against LIDAR snow depth
466 are shown in Fig. 10 and Figs. A7 at 30 m and 90 m resolution and can be contrasted with heatmaps
467 of total snow depth posteriors) against LIDAR snow depth in Figs. 11 and A8 using both single
468 and two-layer retrievals. Note the narrow range of the prior snow depths concentrated around 1.5
469 m and the positive bias relative to LIDAR. The posteriors show much wider range of variability
470 and deeper snow consistent with the LIDAR data for both single and two-layer retrievals, albeit
471 with better agreement for the latter with high counts overlaying the 1:1 line at both spatial

472 resolutions. This behavior is further confirmed by examining the snow depth histograms in Figs.
 473 A9 and A10. The retrievals capture well the range of the LIDAR snow depths for all flights, and
 474 there is a substantial improvement in the shape of the distributions as revealed by the heatmaps.

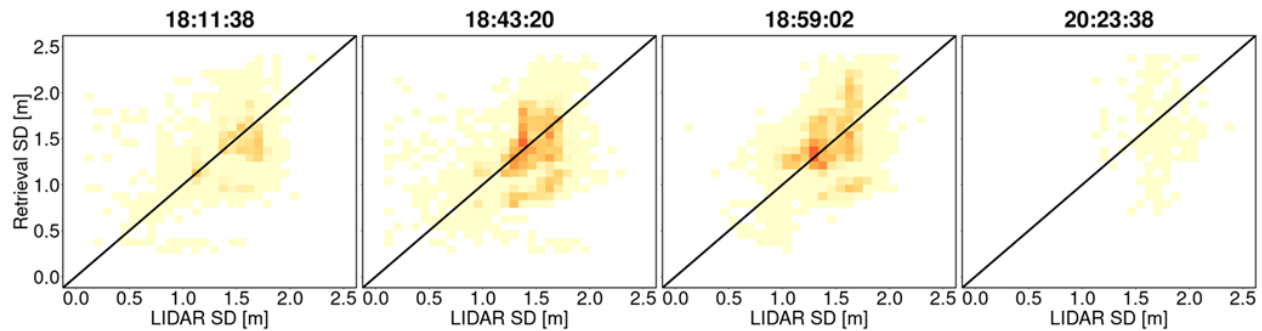
475



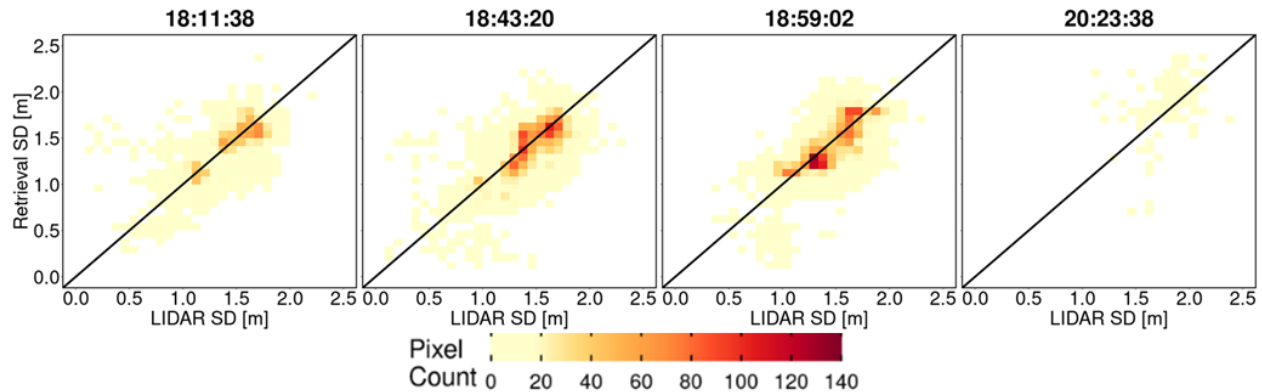
476

477 **Figure 10:** Heatmap of LIDAR and MSHM predicted snow depth priors at 30 m resolution using overlapping pixels from the
 478 MSHM and LIDAR. Only pixels with incidence angle between 30° - 45° , and moderate sub-grid scale variability of LIDAR snow
 479 depth (< 0.3).

a) Single-Layer Snow Depth Retrievals



b) Two-Layer Snow Depth Retrievals



480

481 **Figure 11:** Heatmap of LIDAR versus successful snow depth (SD) retrievals at 30 m resolution using overlapping LIDAR and
 482 retrieval pixels. Successful retrievals are for pixels with local SnowSAR incidence angles in the 30°- 45° range and relative residual
 483 backscatter (RRB) of less than 30% for each of the four flights (see Table 4). LIDAR SD in pixels with subgrid scale variability
 484 corresponding to standard deviation of less than 0.3 m for the upscaled 90 m LIDAR pixel are not included.

485

486 Quantitative assessment metrics are presented in Tables 5 and A1 for the comparison between
 487 various snow depth datasets at 30 and 90 m resolutions, respectively. The snow depth MARE is
 488 higher for the retrievals compared to the priors (MSHM) due to the fact that MARE is an effective
 489 metric capturing distance from the mean. CB20 showed that the MSHM simulated average snow
 490 mass accumulation at the Grand Mesa scale is within 10% of observations at a monthly time-scale
 491 in February 2017. The BC coefficients The BC coefficients of 0.95 and above at 30 m resolution
 492 indicate significant agreement between the shapes of the distributions at 0.95 or above at 30m
 493 resolution using the two-layer retrievals for the west-east flights, and 0.76 for the fourth flight at
 494 20:23:38 GMT over the forested area. There is significant improvement relative to MSHM priors
 495 in the statistical similarity of the snow depth retrievals vis-à-vis the LIDAR data for all cases, and
 496 more so for the fourth flight over the forest. For snow depth, 30 m resolution and two-layer
 497 retrievals outperform the 90 m resolution and single-layer retrievals for all flights. This is
 498 explained in part by landcover classification errors that are smaller at 30 m. Figure A11 shows
 499 that the number of pixels where retrievals produce large mean absolute residuals is very small and
 500 characterize by low confidence in the LIDAR estimates.

501

502 **Table 5:** Summary of statistics and error metrics of the 3 snow depth (SD) data sets at 30 m resolution: LIDAR measurements,
 503 MSHM predictions, and successful SnowSAR retrievals for grassland pixels and subgrid-scale standard deviation (σ) of less than
 504 0.3 m for the upscaled LIDAR pixel. MARE – Mean Absolute Relative Error (Eq. 6); BC – Bhattacharya Coefficient (Eq. 7). Here
 505 mean and standard deviation refer to the spatial distribution, unlike the prior mean and standard deviation used in Base-AM (Table
 506 3). Successful retrievals are for pixels with local incidence angles in the 30°- 45° range and relative residual backscatter (RRB) of
 507 less than 30% for each of the four flights (see Table 4).

Flight (GMT)	N Layer	Spatial SD μ [m]			Spatial SD σ [m]			MARE SD		BC SD	
		Retrieved	MSHM	LIDAR	Retrieved	MSHM	LIDAR	Retrieved-LIDAR	MSHM-LIDAR	Retrieved-LIDAR	MSHM-LIDAR
18:11:38	1	1.39	1.42	1.42	0.32	0.15	0.28	0.19	0.11	0.94	0.67
18:43:20		1.41	1.38	1.42	0.32	0.21	0.27	0.18	0.11	0.96	0.75
18:59:02		1.49	1.38	1.44	0.33	0.20	0.27	0.18	0.09	0.94	0.76
20:23:38		1.66	1.58	1.77	0.36	0.16	0.22	0.21	0.13	0.71	0.25
18:11:38	2	1.38	1.41	1.40	0.30	0.17	0.29	0.14	0.12	0.98	0.67
18:43:20		1.35	1.38	1.42	0.31	0.20	0.28	0.14	0.11	0.97	0.75
18:59:02		1.40	1.38	1.44	0.31	0.20	0.27	0.12	0.09	0.95	0.75
20:23:38		1.89	1.61	1.80	0.39	0.14	0.24	0.17	0.12	0.76	0.23

508

509 Tables 6 and A2 summarize the average absolute relative errors between snowpits and SWE
 510 retrievals from all flights within 100 m of the snowpits. The results are significantly better for two-
 511 layer snowpack retrievals. The mean absolute relative errors at 30 m resolution are 0.22 and 0.13
 512 for 1 layer and 2 layer snowpacks respectively. The mean absolute relative errors at 90 m resolution

513 are 0.2 and 0.12 for 1 layer and 2 layer snowpacks respectively. There is a variable number of
 514 pixels used for the calculation of the error metrics for each snow pit, which in the case of 51S is
 515 so small that it suggests the pit is not in the flight path. The large errors for pits 4500, 44E and and
 516 53W are attributed to very heterogeneous landcover including water and forest (4500), and
 517 proximity to roads (53W and 44E). After removing these snowpits in the central area marked in
 518 Fig. A12, the average absolute relative SWE residuals are 5-7% (15-18%) for the two-layer (single-
 519 layer) retrieval algorithm.

520

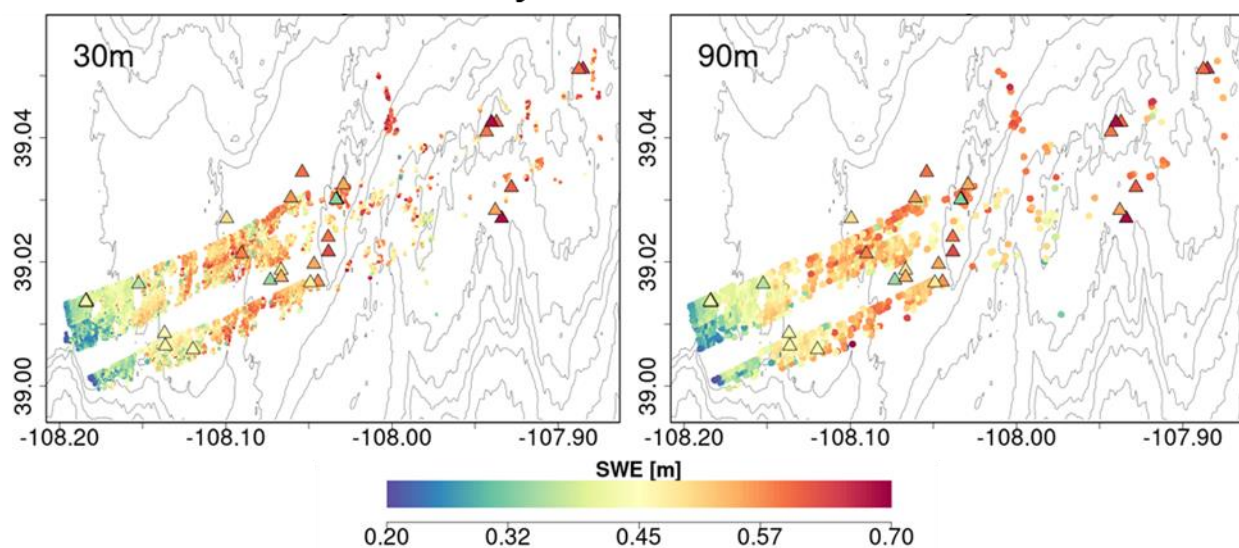
521 **Table 6:** Evaluation of successful SWE retrievals at 30 m resolution against SWE at SnowEx'17 snow pits and
 522 retrieved snowpacks at 30 m resolution. All N pixels with centroids within 100 m of each snow pit are in the Grasslands
 523 (according to the Landcover dataset at 30 m resolution, see Table 1). SD – snow depth. Italicized rows correspond to
 524 large local MARE (Mean Absolute Relative Error, Eq. 6).

Date	x	y	Pit SD (m)	Pit SWE (m)	Retrieved SWE (m)		MARE		N pixels	Avg. Dist (m)	Pit ID
					1 Lyr	2 Lyr	1 Lyr	2 Lyr			
2/20/2017	-108.184	39.014	1.15	0.368	0.455	0.386	0.236	0.049	28	18	KC1C
2/20/2017	-108.184	39.014	1.19	0.386	0.457	0.387	0.184	0.003	27	12	KC1E
2/20/2017	-108.184	39.014	1.18	0.386	0.456	0.387	0.181	0.003	26	15	KC1N
2/20/2017	-108.184	39.013	1.24	0.414	0.456	0.387	0.101	0.065	27	20	KC1S
2/20/2017	-108.184	39.014	1.30	0.435	0.455	0.385	0.046	0.115	29	11	KC1W
2/22/2017	-108.136	39.006	1.32	0.436	0.556	0.484	0.275	0.110	22	8	29E
2/22/2017	-108.090	39.021	1.65	0.583	0.685	0.596	0.175	0.022	19	17	38E
2/22/2017	<i>-108.060</i>	<i>39.030</i>	<i>2.10</i>	<i>0.763</i>	<i>0.368</i>	<i>0.449</i>	<i>0.518</i>	<i>0.412</i>	<i>12</i>	<i>16</i>	<i>53W</i>
2/22/2017	-108.044	39.017	1.68	0.566	0.480	0.505	0.152	0.108	5	51	63E
2/22/2017	-108.049	39.017	1.49	0.48	0.494	0.513	0.029	0.069	13	29	63W
2/22/2017	-108.029	39.032	1.66	0.55	0.558	0.581	0.015	0.056	18	15	67N
2/23/2017	<i>-108.067</i>	<i>39.029</i>	<i>2.13</i>	<i>0.761</i>	<i>0.593</i>	<i>0.504</i>	<i>0.221</i>	<i>0.338</i>	<i>9</i>	<i>23</i>	<i>44E</i>
2/23/2017	<i>-108.061</i>	<i>39.030</i>	<i>1.59</i>	<i>0.568</i>	<i>0.365</i>	<i>0.408</i>	<i>0.357</i>	<i>0.282</i>	<i>3</i>	<i>75</i>	<i>51S</i>
2/24/2017	-108.033	39.030	1.80	0.576	0.657	0.573	0.141	0.005	20	10	0
2/24/2017	-108.033	39.030	1.84	0.598	0.652	0.581	0.090	0.028	21	14	800
2/24/2017	-108.033	39.030	1.80	0.571	0.650	0.581	0.138	0.018	22	19	1390
2/24/2017	-108.033	39.030	1.75	0.566	0.654	0.581	0.155	0.027	21	15	2000
2/24/2017	-108.033	39.030	1.67	0.560	0.654	0.581	0.168	0.037	21	9	2500
2/24/2017	<i>-108.034</i>	<i>39.030</i>	<i>1.12</i>	<i>0.331</i>	<i>0.660</i>	<i>0.580</i>	<i>0.994</i>	<i>0.752</i>	<i>18</i>	<i>19</i>	<i>4500</i>
Mean			1.56	0.52	0.54	0.50	0.22	0.13	19.00	20.84	

525

526 Finally, composite spatial maps of successful SWE retrievals from all flights overlain by the
 527 snowpit measurements between 20-24 February are shown in Fig. 12. Because of the different
 528 viewing geometries, retrievals between incident angles 30°-35° for flight path at 18:59:02 in the
 529 composite of overlapping flight paths at 18:43:20 and 18:59:02 GMT were removed. Note the
 530 consistency at 30 m and 90 m resolutions as well as the overall agreement between SWE at
 531 snowpits and SWE retrievals on the flightlines.

Two-Layer SWE Retrievals



532

533 **Figure 12:** Composite spatial distribution of SWE (2-layer retrievals) successfully retrieved at 30m (left) and 90m (right) resolution
534 for grassland pixels for the four SnowSAR flights. Snow pits (20-24 Feb, Fig. 4, Tables 6) are marked by triangles colored according
535 to SWE. SnowEx'17 snow pit locations are marked by triangles and colored according to SWE. Successful retrievals are for pixels
536 with local incidence angles in the 30°- 45° range and relative residual backscatter (RRB) of less than 30% for each of the four
537 flights (see Table 4). As two flights Gray elevation contours are plotted every 100m.

538

539 6. Conclusion

540 A Bayesian physical-statistical SWE retrieval framework leveraging prior work (CB20, CB23,
541 P17, P23, Fig. 5) was applied to airborne X- and Ku-band measurements yielding robust results
542 from multiple SnowSAR flights over grassland and mixed grassland and forest in Grand Mesa,
543 Colorado. Prior distributions of snowpack parameters were obtained from a multilayer snow
544 hydrology model with atmospheric forcing derived from operational NWP forecasts and analysis
545 (CB20, CB23). In order to reconcile the number of independent measurements, physical
546 constraints, and reduce the number of snowpack parameters, snowpack stratigraphy was mapped
547 into single-layer and two-layer snowpacks and then Bayesian inference using Base-AM was
548 applied (P17, P23). The SnowSAR measurements were averaged to 30 and 90 m resolutions, and
549 retrievals were conducted independently for every measurement pixel along the flight lines.
550 Retrievals for measurements with convergence backscatter relative errors less than 30% (± 1.2 dB)
551 and for incidence angles in the 30°- 45° range were considered successful over grasslands,
552 corresponding to 75 -87% of all retrievals depending on the flight.

553 The retrievals, specifically the local means of the posterior distributions, were evaluated against
554 the spatial distribution of LIDAR snow depth estimates up to 2 m and against snowpit SWE
555 measurements up to 700 mm and snow depth up to 2.13 m. Since the LIDAR and snowpit
556 measurements were not concurrent with the SnowSAR flights, the assessment of retrieval skill was
557 conducted over a period of five days without snowfall or significant day-to-day weather changes.
558 The two-layer snowpack retrievals perform better overall capturing the observed spatial gradients

559 of snow depth, with SWE relative errors $\leq 7\%$ as compared with 18% for single-layer SWE
560 retrievals, and snow depth absolute retrieval residuals 10-20% depending on landcover
561 heterogeneity and measurement uncertainty. The statistical structure of retrieved snow depth is
562 similar to that estimated by LIDAR, which is indicative of the retrievals ability to capture snow
563 patterns and scaling behavior to support scientific process studies. For satellite-based monitoring
564 from space in the context of a future snow mission, time-series of measurements would be
565 available that should improve the estimates of the priors based on antecedent information. This is
566 not possible for one-time observations during field experiments such as SnowEx'17, and thus
567 improved results would be expected under realistic satellite-based applications. NWP forecasts
568 are available worldwide and therefore this retrieval framework can be applied to SAR
569 measurements anywhere.

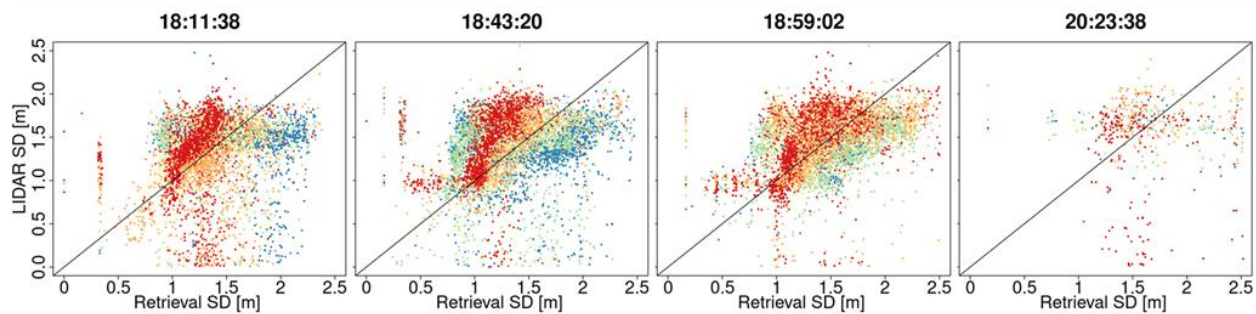
570 The radar model used in this study (MEMLS) does incorporate snow-ground-vegetation scattering
571 interactions. Grassland vegetation during the accumulation season is assumed to be submerged
572 and the impact of vegetation is included in the estimation of the background backscatter (σ_{bkg} , Fig.
573 1). Because the landcover data are categorical, in addition to the uncertainty of the data at 30 m
574 resolution, additional uncertainty is tied to the selection of homogeneous grassland pixels at 90
575 resolution, which explains some of the unsuccessful retrievals especially along the grassland-
576 forest, shrub and wetland boundaries. The potential for estimating σ_{bkg} independently for each
577 location as proposed by Cao and Barros (2023b) provides an alternative to simplify the retrieval
578 workflow and target the Bayesian inference to the snowmass and volume backscatter ($\sigma_{\text{vol}} = \sigma_{\text{total}} -$
579 σ_{bkg}).

580 Airborne measurements are characterized by large changes in viewing geometry across the flight-
581 line and due to other factors such as variable winds and turbulence depending on weather
582 conditions, thus pointing to improved skill from satellite platforms. Building on previous mission
583 concepts (e.g. Rott et al. 2012) and leveraging substantial theory advances and field campaigns in
584 the last decade, this study demonstrates the utility and effectiveness of X- and Ku-band SAR
585 technology to remotely monitor snowmass at high spatial resolution and with accuracy and
586 uncertainty that meet the requirements expressed in the most recent Earth Science and Applications
587 from Space Decadal Survey (NASSEM, 2018).

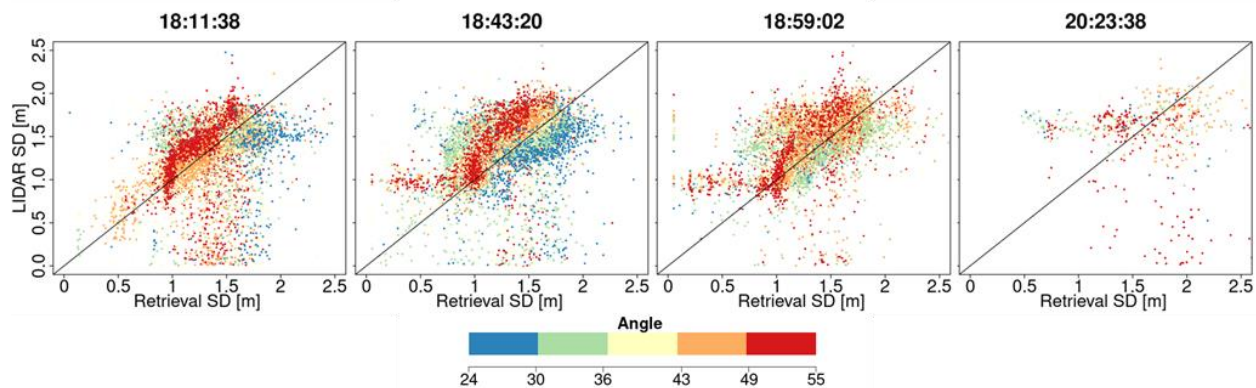
588
589
590
591
592
593
594
595

Sensitivity to Incidence Angle

a) Single-Layer Depth Retrieval



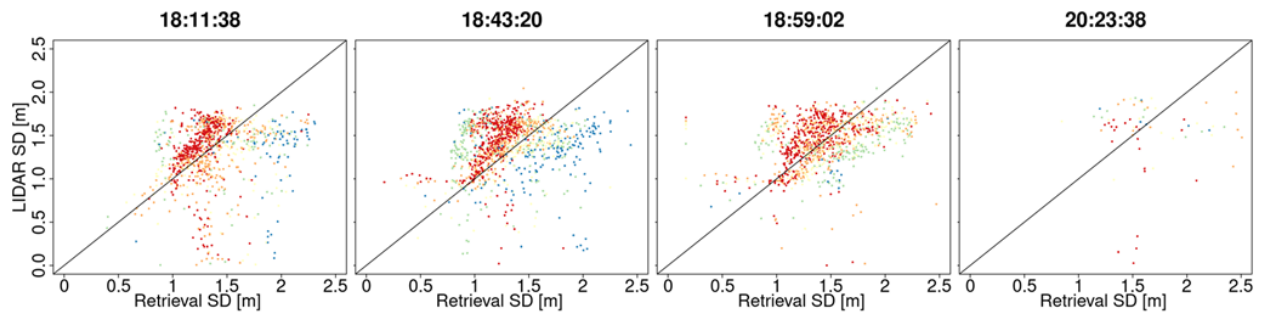
b) Two-Layer Depth Retrieval



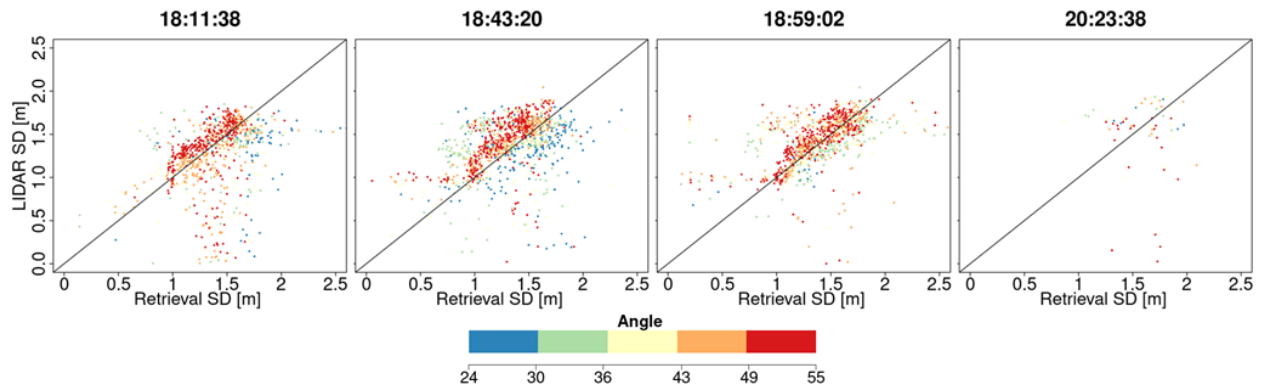
600 **Figure A1:** Same as Fig. 7b with pixels color coded according to the local SnowSAR incidence angle for all four flightlines and
601 for single-(top row) and two-layer (bottom row) retrievals at 30 m resolution.

Sensitivity to Incidence Angle

a) Single-Layer Depth Retrieval



b) Two-Layer Depth Retrieval



602

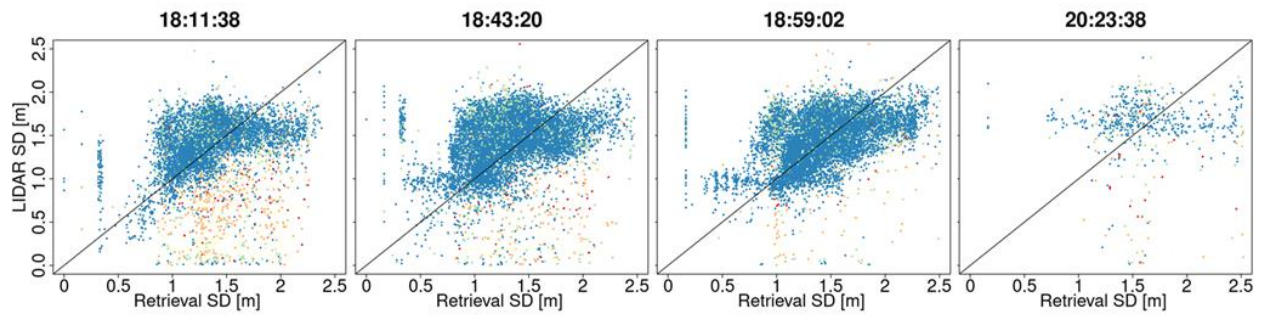
603 **Figure A2:** Same as Fig. 7b with pixels color coded according to the local SnowSAR incidence angle for all four flightlines and
604 for single-(top row) and two-layer (bottom row) retrievals at 90 m resolution.

605

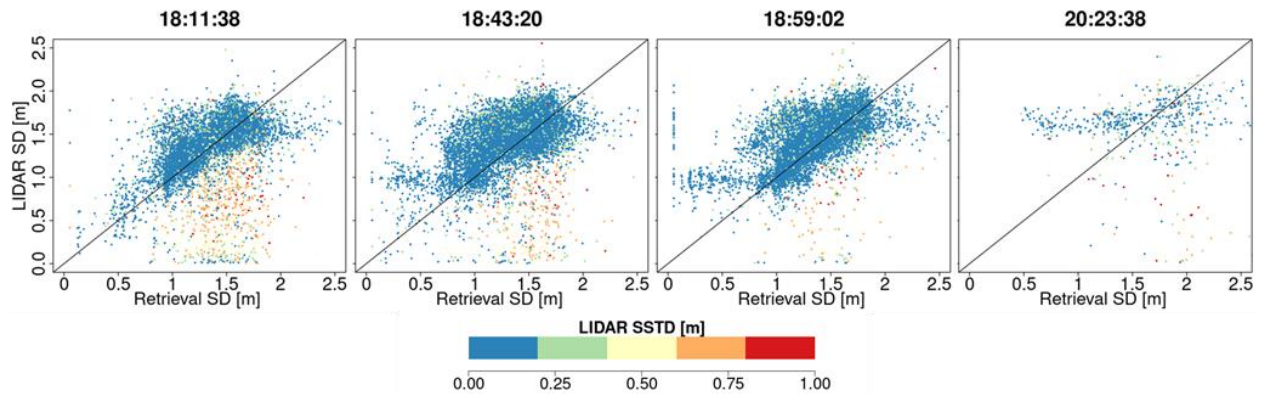
606

Sensitivity to Spatial Variability

a) Single-Layer Depth Retrieval



b) Two-Layer Depth Retrieval



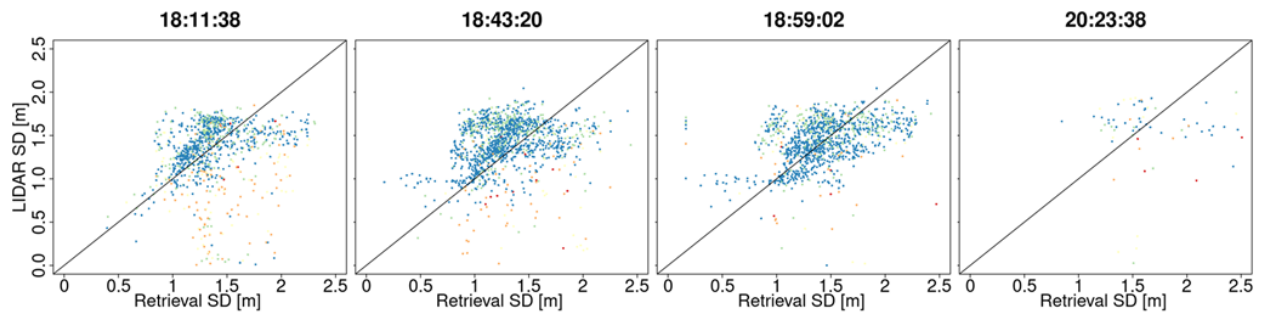
607

608 **Figure A3:** Comparison between LIDAR snow depth (SD) and successful retrievals for single and two-layer algorithms. The
609 pixels are color coded according to the subgrid scale variability of the 30 m upscaled LIDAR pixel.

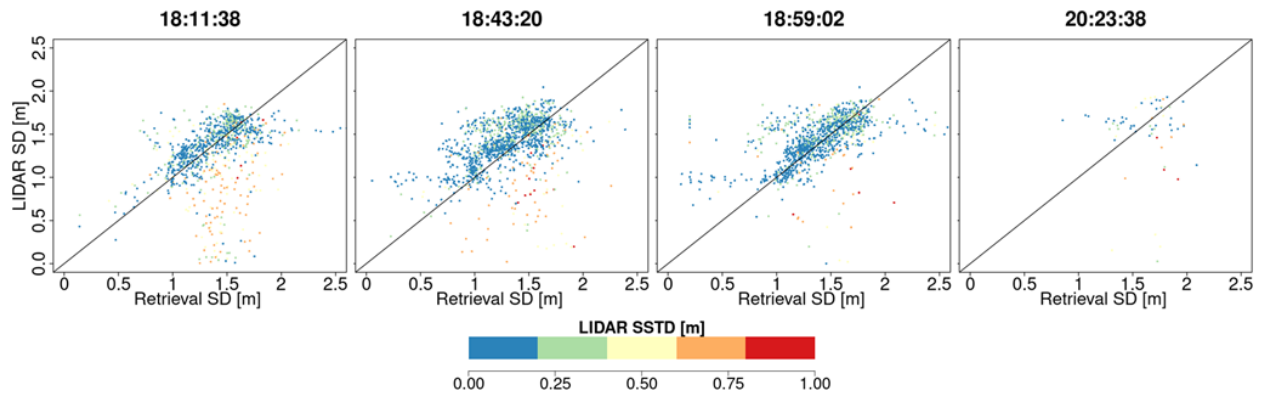
610

Sensitivity to Spatial Variability

a) Single-Layer Depth Retrieval



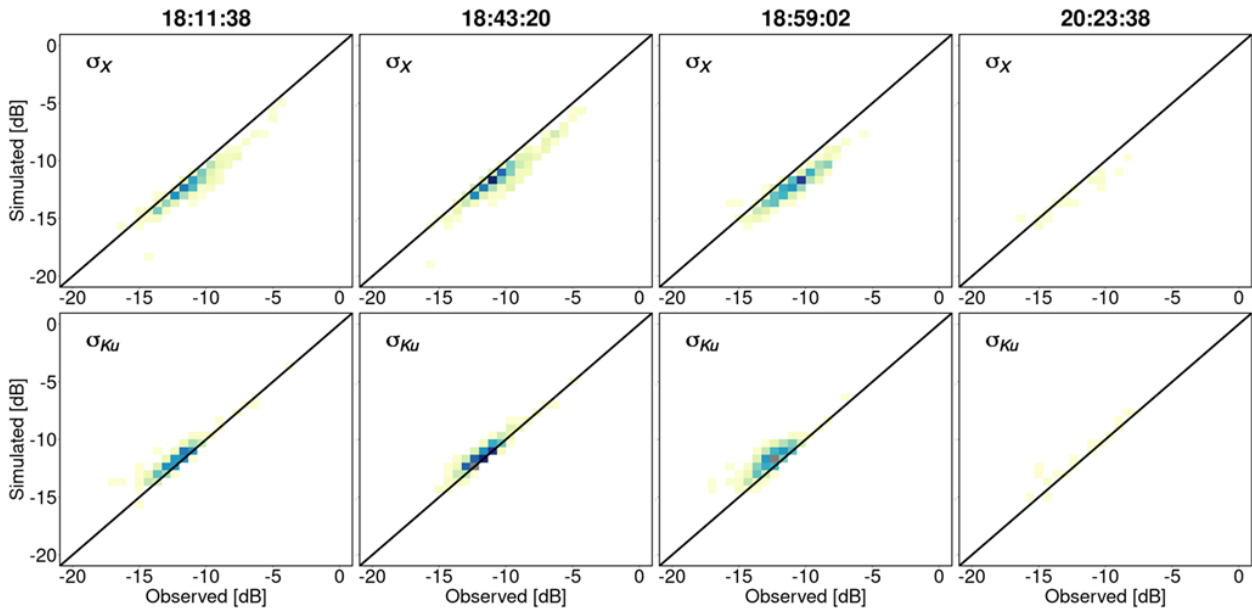
b) Two-Layer Depth Retrieval



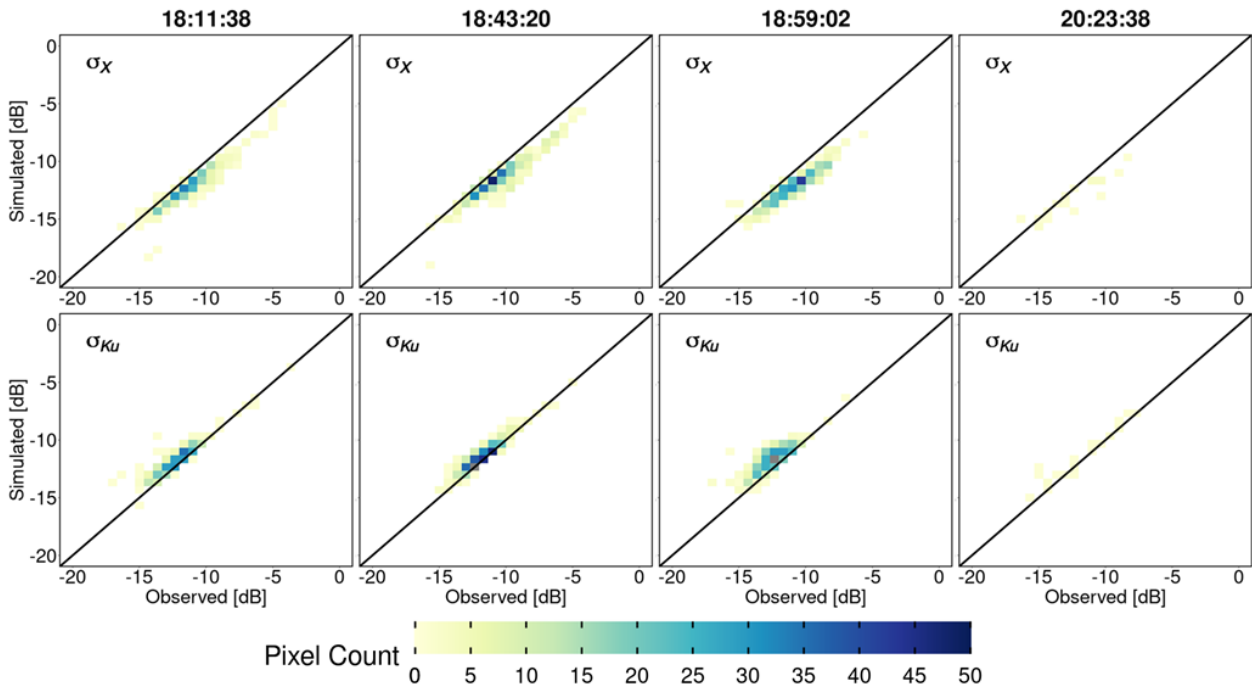
611

612 **Figure A4:** Comparison between SnowSAR snow depth and successful retrievals. The pixels are color coded according to the
613 subgrid scale variability of the 90 m upscaled LIDAR pixel.

a) Single-Layer Retrievals



b) Two-Layer Retrievals

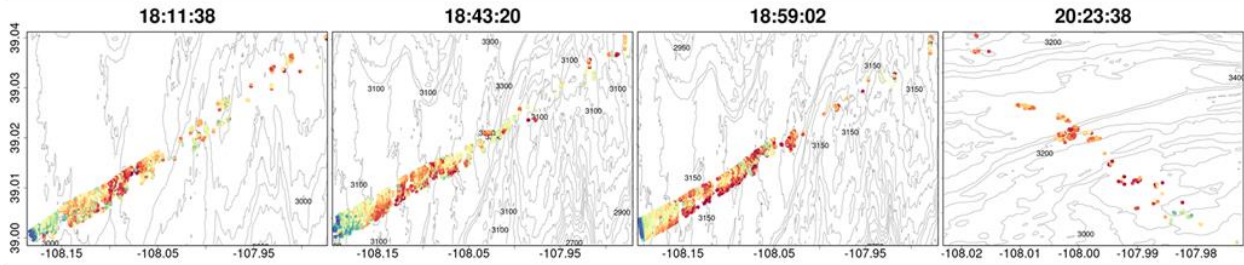


614

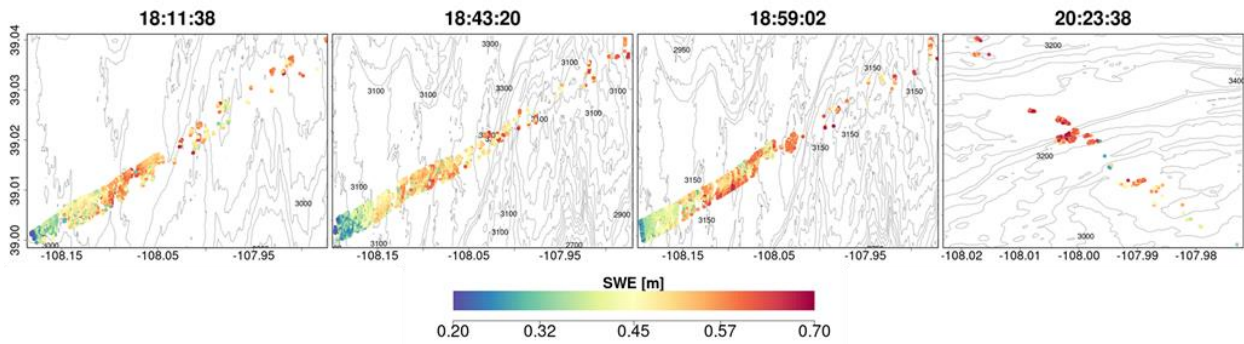
615 **Figure A5:** Heatmaps of SnowSAR backscatter measurements (observed) versus retrievals (simulated) backscatter at 90 m
 616 resolution: a) single-layer snowpack; b) 2-layer snowpack for X- (σ_X) and Ku- (σ_{Ku}) bands. Successful retrievals are for pixels
 617 with local incidence angles in the 30°- 45° range and relative residual backscatter (RRB) of less than 30% for each of the four
 618 flights (see Table 4).

619

a) Single-Layer SWE Retrievals



b) Two-Layer SWE Retrievals

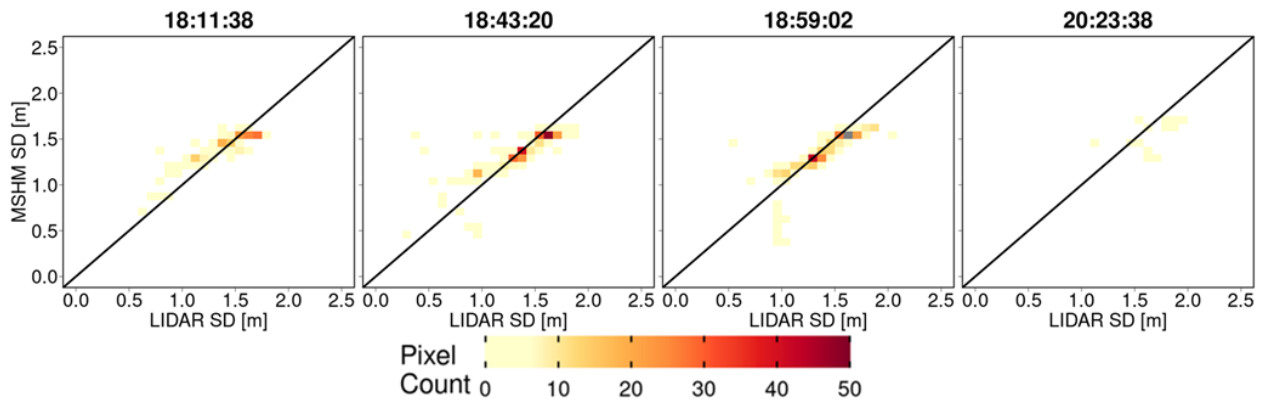


620

621 **Figure A6** Spatial distribution of successful SWE retrievals for 1-layer (a) and 2-layer (b) snowpacks in grassland pixels at 90 m
 622 resolution. Successful retrievals are for pixels with local incidence angles in the 30°- 45° range and relative residual backscatter
 623 (RRB) of less than 30% for each of the four flights (see Table 4).

624

MSHM Snow Depth Simulation

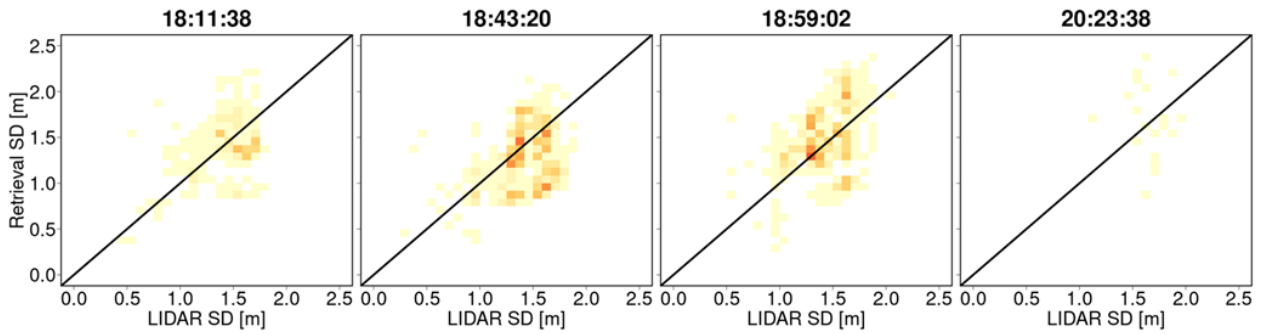


625

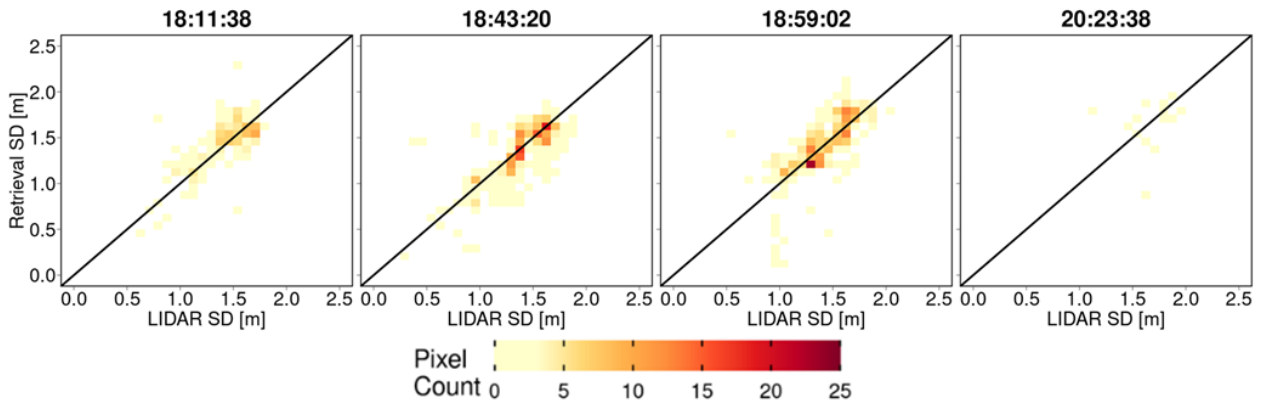
626 **Figure A7:** Heatmaps of LIDAR snow depth and snow depth predicted by MSHM at the time of SnowSAR flights for
 627 overlapping pixels at 90 m resolution.

628

a) Single-Layer Snow Depth Retrievals



b) Two-Layer Snow Depth Retrievals



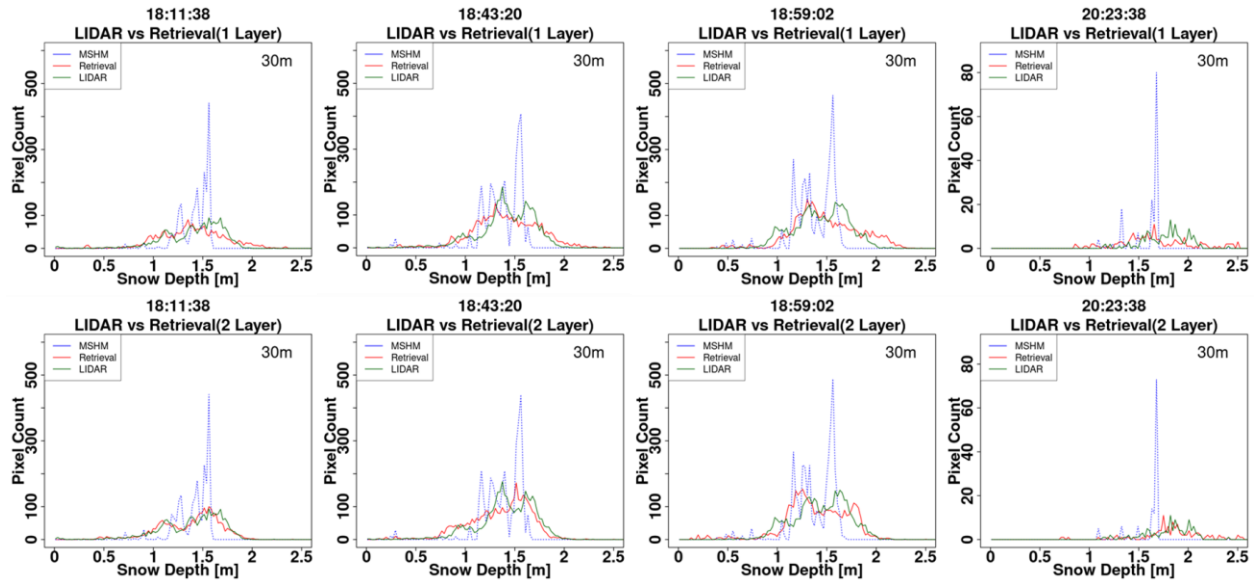
629

630 **Figure A8:** Heatmaps of LIDAR versus successful snow depth (SD) retrievals at 90 m resolution using overlapping LIDAR and
 631 retrieval pixels. Successful retrievals are for pixels with local SnowSAR incidence angles in the 30°- 45° range and relative residual
 632 backscatter (RRB) of less than 30% for each of the four flights (see Table 4). LIDAR SD in pixels with subgrid scale variability
 633 corresponding to standard deviation of less than 0.3 m for the upscaled 90 m LIDAR pixel are not included.

634

635

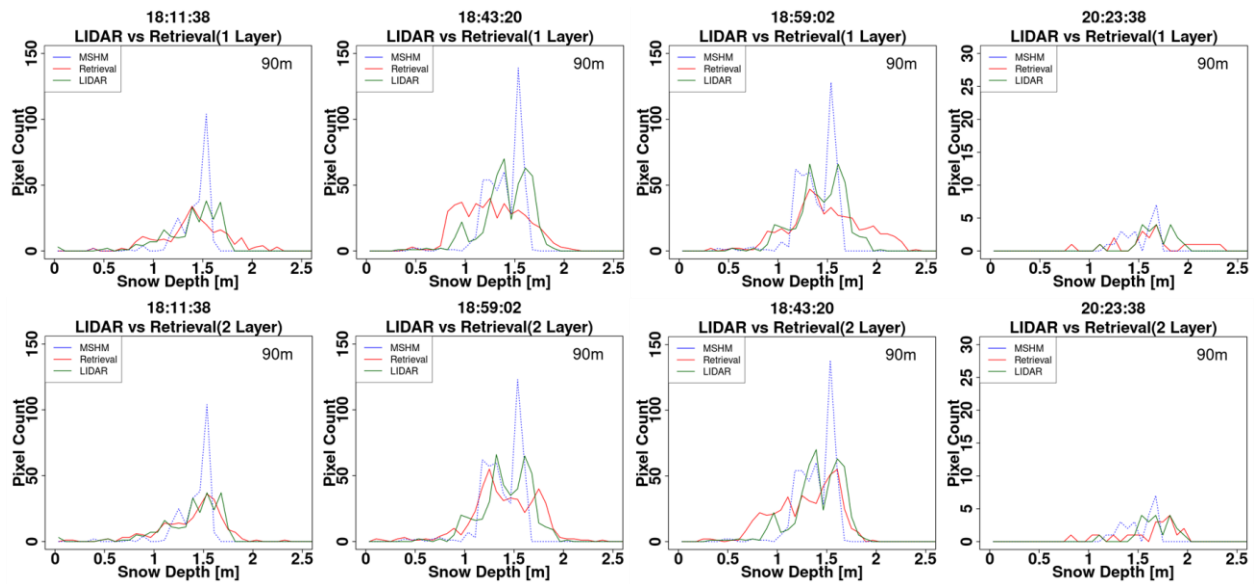
636



637

638 **Figure A9:** Histogram of snow depth (SD) from LIDAR, MSHM, and successful retrievals at 30 m using 1- and 2- layer
 639 snowpacks. The total number of pixels for each snow depth product is the same. Successful retrievals are for pixels with local
 640 incidence angles in the 30°- 45° range and relative residual backscatter (RRB) of less than 30% for each of the four flights (see
 641 Table 4). LIDAR SD in pixels with subgrid scale variability corresponding to standard deviation of less than 0.3 m for the
 642 upscaled 90 m LIDAR pixel are not included.

643



644

645 **Figure A10 -** Histogram of snow depth (SD) from LIDAR, MSHM, and successful retrievals at 90 m using 1- and 2- layer
 646 snowpacks. The total number of pixels for each snow depth product is the same. Successful retrievals are for pixels with local
 647 incidence angles in the 30°- 45° range and relative residual backscatter (RRB) of less than 30% for each of the four flights (see
 648 Table 4). LIDAR SD in pixels with subgrid scale variability corresponding to standard deviation of less than 0.3 m for the
 649 upscaled 90 m LIDAR pixel are not included.

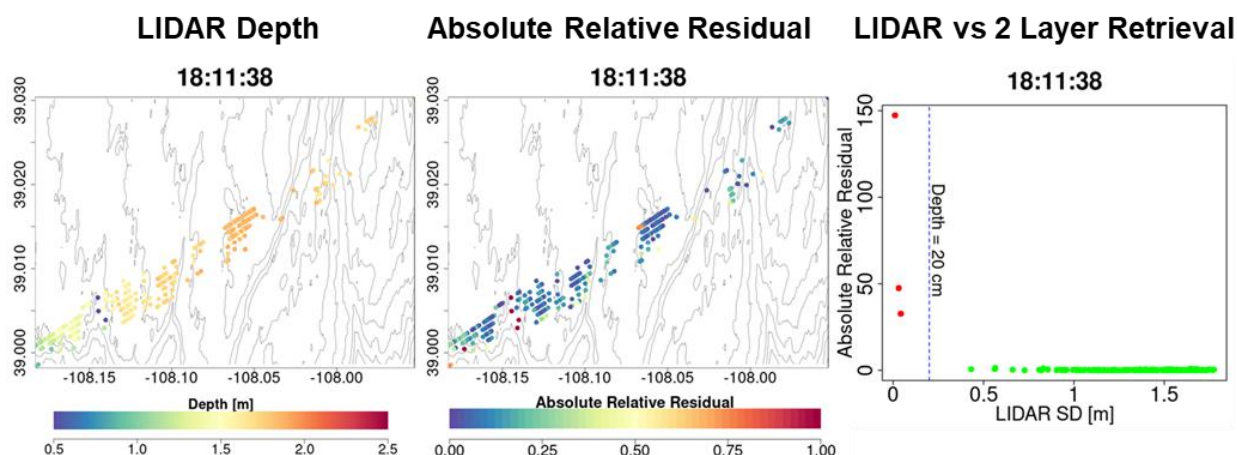
650

651

652 **Table A1** – Same as Table 5 but for resolution of 90 m.

Flight (GMT)	N Layer	Spatial SD μ [m]			Spatial SD σ [m]			MARE SD		BC SD	
		Retrieved	MSHM	LIDAR	Retrieved	MSHM	LIDAR	Retrieved-LIDAR	MSHM-LIDAR	Retrieved-LIDAR	MSHM-LIDAR
18:11:38	1	1.41	1.42	1.40	0.33	0.18	0.26	0.19	0.09	0.90	0.78
18:43:20		1.27	1.39	1.41	0.32	0.19	0.25	0.21	0.08	0.90	0.85
18:59:02		1.48	1.38	1.42	0.37	0.20	0.25	0.21	0.07	0.90	0.82
20:23:38		1.68	1.52	1.66	0.38	0.17	0.19	0.24	0.12	0.66	0.50
18:11:38	2	1.41	1.42	1.40	0.35	0.18	0.26	0.15	0.09	0.95	0.77
18:43:20		1.29	1.39	1.41	0.32	0.19	0.25	0.16	0.08	0.92	0.85
18:59:02		1.41	1.38	1.42	0.35	0.20	0.25	0.15	0.07	0.92	0.82
20:23:38		1.67	1.52	1.66	0.45	0.17	0.19	0.22	0.12	0.76	0.50

653



654

655 **Figure A11** - Analysis of unsuccessful retrievals for pixels with large mean snow depth residuals at 90 m resolution: a) Map of
 656 LIDAR snow depth highlighting in deep blue the locations where very shallow snow is attributed to measurement error. b) Note
 657 spatial agreement between shallow snow depth and very large residuals. c) There are only a few points at the edges of forests and
 658 shallow snow depths that are flagged not successful. The gray elevation contours are plotted every 50 m.

659

660

661

662

663

664

665

666

667

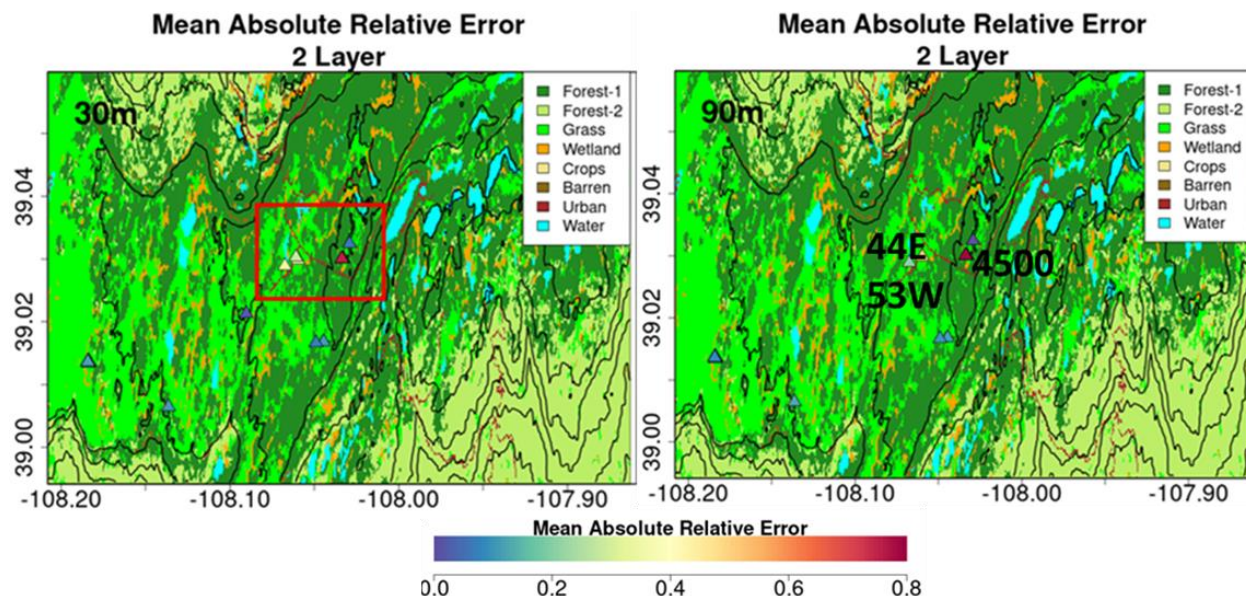
668

669 **Table A2:** Same as Table 7 but for resolution of 90 m.

Date	x	y	Pit SD (m)	Pit SWE (m)	Retrieved SWE (m)		Mean Abs Rel Error		N pixels	Avg. Dist (m)	Pit ID
					1 Lyr	2 Lyr	1 Lyr	2 Lyr			
2/20/2017	-108.184	39.014	1.15	0.368	0.473	0.398	0.29	0.08	4	18	KC1C
2/20/2017	-108.184	39.014	1.19	0.386	0.471	0.397	0.22	0.03	3	12	KC1E
2/20/2017	-108.184	39.014	1.18	0.386	0.473	0.399	0.22	0.03	2	29	KC1N
2/20/2017	-108.184	39.013	1.24	0.414	0.474	0.398	0.15	0.04	3	27	KC1S
2/20/2017	-108.184	39.014	1.3	0.435	0.476	0.399	0.09	0.08	3	47	KC1W
2/22/2017	-108.136	39.006	1.32	0.436	0.572	0.490	0.31	0.12	2	39	29E
2/22/2017	-108.060	39.030	2.10	0.763	0.340	0.384	0.55	0.50	1	43	53W
2/22/2017	-108.044	39.017	1.68	0.566	0.454	0.499	0.20	0.12	1	75	63E
2/22/2017	-108.049	39.017	1.49	0.480	0.521	0.530	0.09	0.10	1	29	63W
2/22/2017	-108.029	39.032	1.66	0.550	0.529	0.553	0.04	0.01	4	47	67N
2/23/2017	-108.067	39.029	2.13	0.761	0.751	0.606	0.01	0.20	1	70	44E
2/24/2017	-108.033	39.030	1.8	0.576	0.718	0.601	0.25	0.04	3	60	0
2/24/2017	-108.033	39.030	1.84	0.598	0.717	0.600	0.20	0.00	2	57	800
2/24/2017	-108.033	39.030	1.80	0.571	0.717	0.600	0.26	0.05	2	55	1390
2/24/2017	-108.033	39.030	1.75	0.566	0.687	0.592	0.21	0.05	1	54	2000
2/24/2017	-108.033	39.030	1.67	0.560	0.687	0.592	0.23	0.06	1	54	2500
2/24/2017	-108.034	39.030	1.12	0.331	0.687	0.592	1.08	0.79	1	62	4500
2/20/2017	-108.184	39.014	1.15	0.368	0.473	0.398	0.29	0.08	4	18	KC1C
2/20/2017	-108.184	39.014	1.19	0.386	0.471	0.397	0.22	0.03	3	12	KC1E
Mean			1.51	0.50	0.56	0.50	0.26	0.13	2.21	42.53	

670

671



672

673 **Figure A12** – Spatial context for snow pits with very large absolute relative errors (MARE) calculated as the mean of the
 674 relative difference between SWE retrievals within 100 m of the snow pit and the values at the snow pit. Locations with very large
 675 errors (orange to red) are inside the red box marked in top plot. Snowpit 4500 is a region of complex land cover including
 676 evergreen forest, a road and a pond. Snowpits 53W and 44E are close to each other on the same side of the road in expansive
 677 grassland.

678 **8. Data Availability**

679 Links to access all datasets used in this study are provided in Table 1.

680

681 **9. Author Contribution**

682 AB and MD conceptualized the study; SS developed and implemented the retrieval framework
683 including modifications and coupling of the codes under the guidance of AB; SS completed the
684 retrievals and analyzed the results under the guidance of AB with input from MD; MD provided
685 the original code of the Base-AM model; AB provided the original MSHM code; EK curated the
686 SnowSAR dataset; SS and APB wrote the paper and replied to Reviewers with comments from
687 MD and EK.

688

689 **10. Competing Interests**

690 The contact author has declared that none of the authors has any competing interests

691

692 **11. References**

693 Bateni, S. M., Margulis, S. A., Podest, E., and McDonald, K. C.: Characterizing Snowpack and
694 the Freeze–Thaw State of Underlying Soil via Assimilation of Multifrequency Passive/Active
695 Microwave Data: A Case Study (NASA CLPX 2003), *IEEE Trans. Geosci. Remote Sens.*, 53,
696 173–189, <https://doi.org/10.1109/TGRS.2014.2320264>, 2015.

697 Benjamin, S. G., Weygandt, S. S., Brown, J. M., Hu, M., Alexander, C. R., Smirnova, T. G., Olson,
698 J. B., James, E. P., Dowell, D. C., Grell, G. A., Lin, H., Peckham, S. E., Smith, T. L., Moninger,
699 W. R., Kenyon, J. S., and Manikin, G. S.: A North American Hourly Assimilation and Model
700 Forecast Cycle: The Rapid Refresh, *Mon. Weather Rev.*, 144, 1669–1694,
701 <https://doi.org/10.1175/MWR-D-15-0242.1>, 2016.

702 Berliner, L. M.: Physical-statistical modeling in geophysics: Physical-Statistical Modeling in
703 Geophysics, *J. Geophys. Res. Atmospheres*, 108, n/a-n/a, <https://doi.org/10.1029/2002JD002865>,
704 2003.

705 Bhattacharyya, A.: On a measure of divergence between two statistical populations defined by
706 their probability distributions". <https://doi.org/10.3390/rs12203422>, 2020.

707 Cao, Y. and Barros, A.P.: Weather-Dependent Nonlinear Microwave Behavior of Seasonal High-
708 Elevation Snowpacks, *Remote Sens.*, 12, 3422, <https://doi.org/10.3390/rs12203422>, 2020.

709 Cao, Y. and Barros, A. P.: Topographic controls on active microwave behavior of mountain
710 snowpacks, *Remote Sens. Environ.*, 284, 113373, <https://doi.org/10.1016/j.rse.2022.113373>,
711 2023a.

712 Cao, Y. and Barros, A. P.: Indirect Estimation of Vegetation Contribution to Microwave
713 Backscatter Via Triple-Frequency SAR Data, in: IGARSS 2023 - 2023 IEEE International
714 Geoscience and Remote Sensing Symposium, Pasadena, CA, USA, 3114–3117,
715 <https://doi.org/10.1109/IGARSS52108.2023.10281754>, 2023b.

716 Deems, J. S., Painter, T. H., and Finnegan, D. C.: Lidar measurement of snow depth: a review, *J.*
717 *Glaciol.*, 59, 467–479, <https://doi.org/10.3189/2013JoG12J154>, 2013.

718 Dobson, M., Ulaby, F., Hallikainen, M., and El-rayes, M.: Microwave Dielectric Behavior of
719 Wet Soil-Part II: Dielectric Mixing Models, *IEEE Trans. Geosci. Remote Sens.*, GE-23, 35–46,
720 <https://doi.org/10.1109/TGRS.1985.289498>, 1985.

721 Dobson, M., Ulaby, F., Hallikainen, M., and El-rayes, M.: Microwave Dielectric Behavior of
722 Wet Soil-Part II: Dielectric Mixing Models, *IEEE Trans. Geosci. Remote Sens.*, GE-23, 35–46,
723 <https://doi.org/10.1109/TGRS.1985.289498>, 1985.

724 Hallikainen, M., Ulaby, F., Dobson, M., El-rayes, M., and Wu, L.: Microwave Dielectric
725 Behavior of Wet Soil-Part 1: Empirical Models and Experimental Observations, *IEEE Trans.*
726 *Geosci. Remote Sens.*, GE-23, 25–34, <https://doi.org/10.1109/TGRS.1985.289497>, 1985.

727 Huang, X. and Swain, D. L.: Climate change is increasing the risk of a California megaflood, *Sci.*
728 *Adv.*, 8, eabq0995, <https://doi.org/10.1126/sciadv.abq0995>, 2022.

729 Jacobs, J. M., Hunsaker, A. G., Sullivan, F. B., Palace, M., Burakowski, E. A., Herrick, C., and
730 Cho, E.: Snow depth mapping with unpiloted aerial system lidar observations: a case study in
731 Durham, New Hampshire, United States, *The Cryosphere*, 15, 1485–1500,
732 <https://doi.org/10.5194/tc-15-1485-2021>, 2021.

733 Kang, D. H. and Barros, A. P.: Observing System Simulation of Snow Microwave Emissions Over
734 Data Sparse Regions—Part I: Single Layer Physics, *IEEE Trans. Geosci. Remote Sens.*, 50, 1785–
735 1805, <https://doi.org/10.1109/TGRS.2011.2169073>, 2012a.

736 Kang, D. H. and Barros, A. P.: Observing System Simulation of Snow Microwave Emissions
737 Over Data Sparse Regions—Part II: Multilayer Physics, *IEEE Trans. Geosci. Remote Sens.*, 50,
738 1806–1820, <https://doi.org/10.1109/TGRS.2011.2169074>, 2012b.

739 Kim, E., Gatebe, C., Hall, D., Newlin, J., Misakonis, A., Elder, K., Marshall, H. P., Hiemstra, C.,
740 Brucker, L., De Marco, E., Crawford, C., Kang, D. H., and Entin, J.: NASA’s snowex campaign:
741 Observing seasonal snow in a forested environment, in: 2017 IEEE International Geoscience and
742 Remote Sensing Symposium (IGARSS), 2017 IEEE International Geoscience and Remote
743 Sensing Symposium (IGARSS), Fort Worth, TX, 1388–1390,
744 <https://doi.org/10.1109/IGARSS.2017.8127222>, 2017.

745 Kim, R. S., Durand, M., Li, D., Baldo, E., Margulis, S. A., Dumont, M., and Morin, S.: Estimating
746 alpine snow depth by combining multifrequency passive radiance observations with ensemble
747 snowpack modeling, *Remote Sens. Environ.*, 226, 1–15, <https://doi.org/10.1016/j.rse.2019.03.016>,
748 2019.

749 Kuhnert, P. M. (2017). Physical-statistical modeling. In Wiley StatsRef: Statistics Reference
750 Online, pages 1–5. Wiley.

751 Li, D., Durand, M., and Margulis, S. A.: Estimating snow water equivalent in a Sierra Nevada
752 watershed via spaceborne radiance data assimilation, *Water Resour. Res.*, 53, 647–671,
753 <https://doi.org/10.1002/2016WR018878>, 2017.

754 Lowman, L., and Barros, A.P.: Investigating links between climate and orography in the central
755 Andes: Coupling erosion and precipitation using a physical-statistical model, *J. Geophys. Res.*
756 *Earth Surf.*, 119, 1322-1353, <https://doi.org/10.1002/2013JF002940>.

757 Manickam, S. and Barros, A.: Parsing Synthetic Aperture Radar Measurements of Snow in
758 Complex Terrain: Scaling Behaviour and Sensitivity to Snow Wetness and Landcover, *Remote*
759 *Sens.*, 12, 483, <https://doi.org/10.3390/rs12030483>, 2020.

760 Martinec, J., Seidel, K., Burkart, U., and Baumann, R.: Areal modelling of snow water equivalent
761 based on remote sensing techniques., XX General Assembly IUGG in Vienna, 1991.

762 Mendoza, P. A., Musselman, K. N., Revuelto, J., Deems, J. S., López-Moreno, J. I., and McPhee,
763 J.: Interannual and Seasonal Variability of Snow Depth Scaling Behavior in a Subalpine
764 Catchment, *Water Resour. Res.*, 56, <https://doi.org/10.1029/2020WR027343>, 2020.

765 Metropolis, N., Rosenbluth, A.W., Rosenbluth, M., N., Teller, A., and Teller, E.: Equation of State
766 Calculations by Fast Computing Machines. *The Journal of Chemical Physics*, 21, 1087-1092,
767 <https://doi.org/10.1063/1.1699114>, 1953.

768 Mote, T. L., Grundstein, A. J., Leathers, D. J., and Robinson, D. A.: A comparison of modeled,
769 remotely sensed, and measured snow water equivalent in the northern Great Plains: Comparison
770 of Snow Water Equivalent, *Water Resour. Res.*, 39, <https://doi.org/10.1029/2002WR001782>,
771 2003.

772 Musselman, K. N., Addor, N., Vano, J. A., and Molotch, N. P.: Winter melt trends portend
773 widespread declines in snow water resources, *Nat. Clim. Change*, 11, 418–424,
774 <https://doi.org/10.1038/s41558-021-01014-9>, 2021.

775 National Academies of Sciences, Engineering, and Medicine: Thriving on Our Changing Planet:
776 A Decadal Strategy for Earth Observation from Space. Washington, DC: The National Academies
777 Press. <https://doi.org/10.17226/24938>, 2018.

778 Painter, Thomas H., Berisford, Daniel F., Boardman, Joseph W., Bormann, Kathryn J., Deems,
779 Jeffrey S., Gehrke, Frank, Joyce, Michael, Laidlaw, Ross, Mattmann, Chris, McGurk, Bruce,
780 Ramirez, Paul, Richardson, Megan, and Skiles, S. McKenzie: ASO L4 Lidar Snow Depth 3m
781 UTM Grid, Version 1, <https://doi.org/10.5067/KIE9QNVG7HP0>, 2018.

782 Pan, J., Durand, M. T., Vander Jagt, B. J., and Liu, D.: Application of a Markov Chain Monte
783 Carlo algorithm for snow water equivalent retrieval from passive microwave measurements,
784 *Remote Sens. Environ.*, 192, 150–165, <https://doi.org/10.1016/j.rse.2017.02.006>, 2017.

785 Pan, J., Durand, M., Lemmetyinen, J., Liu, D., and Shi, J.: Snow water equivalent retrieved from
786 X- and dual Ku-band scatterometer measurements at Sodankylä using the Markov Chain Monte
787 Carlo method, *The Cryosphere Discuss.* [preprint], <https://doi.org/10.5194/tc-2023-85>, in review,
788 2023.

789 Proksch, M., Mätzler, C., Wiesmann, A., Lemmetyinen, J., Schwank, M., Löwe, H., and
790 Schneebeli, M.: MEMLS3&a: Microwave Emission Model of Layered Snowpacks adapted to
791 include backscattering, *Geosci. Model Dev.*, 8, 2611–2626, [https://doi.org/10.5194/gmd-8-2611-](https://doi.org/10.5194/gmd-8-2611-2015)
792 2015, 2015.

793 Rott, H., Cline, D. W., Duguay, C., Essery, R., Etchevers, P., Hajnsek, I., Kern, M., Macelloni,
794 G., Malnes, E., Pulliainen, J., and Yueh, S. H.: CoReH2O, a dual frequency radar mission for
795 snow and ice observations, in: 2012 IEEE International Geoscience and Remote Sensing
796 Symposium, IGARSS 2012 - 2012 IEEE International Geoscience and Remote Sensing
797 Symposium, Munich, Germany, 5550–5553, <https://doi.org/10.1109/IGARSS.2012.6352348>,
798 2012.

799 Sturm, M., Taras, B., Liston, G. E., Derksen, C., Jonas, T., and Lea, J.: Estimating Snow Water
800 Equivalent Using Snow Depth Data and Climate Classes, *J. Hydrometeorol.*, 11, 1380–1394,
801 <https://doi.org/10.1175/2010JHM1202.1>, 2010.

802 Tsang, L., Durand, M., Derksen, C., Barros, A. P., Kang, D.-H., Lievens, H., Marshall, H.-P., Zhu,
803 J., Johnson, J., King, J., Lemmetyinen, J., Sandells, M., Rutter, N., Siqueira, P., Nolin, A.,
804 Osmanoglu, B., Vuyovich, C., Kim, E., Taylor, D., Merkouriadi, I., Brucker, L., Navari, M.,
805 Dumont, M., Kelly, R., Kim, R. S., Liao, T.-H., Borah, F., and Xu, X.: Review article: Global
806 monitoring of snow water equivalent using high-frequency radar remote sensing, *The Cryosphere*,
807 16, 3531–3573, <https://doi.org/10.5194/tc-16-3531-2022>, 2022.

808 Villano, M., Ustalli, N., Dell’Amore, L., Jeon, S.-Y., Krieger, G., Moreira, A., Peixoto, M. N., and
809 Krecke, J.: NewSpace SAR: Disruptive Concepts for Cost-Effective Earth Observation Missions,
810 in: 2020 IEEE Radar Conference (RadarConf20), 2020 IEEE Radar Conference (RadarConf20),
811 Florence, Italy, 1–5, <https://doi.org/10.1109/RadarConf2043947.2020.9266694>, 2020.

812 Wiesmann, A. and Mätzler, C.: Microwave Emission Model of Layered Snowpacks, *Remote Sens.*
813 *Environ.*, 70, 307–316, [https://doi.org/10.1016/S0034-4257\(99\)00046-2](https://doi.org/10.1016/S0034-4257(99)00046-2), 1999.

817